Paleohydrology of North American Catchments and Rivers at the Onset of the Eocene-Oligocene Climate Transition: Reconstructions from Fluvial Strata of the White River Group, Toadstool Geologic Park, Nebraska

Anjali M. Fernandes[1], Michael T Hren[2], Queenie Chang[1], Virginia B. Smith[3], Baylee McGinnis[2], Dennis O. Terry, Jr.[4], David B. Luffman[1], Mia M. Rhodes[1], Yvette Eley[2], Madelyn A. Kurtz[1], Sarah E. Heithaus[1]

Corresponding author: Dr. Anjali M. Fernandes, Email: anjali.fernandes@denison.edu

This is a non peer-reviewed pre-print submitted to EarthArXiv, and in review at the Bulletin of the Geological Society of America

Paleohydrology of North American Catchments and Rivers at the Onset of the Eocene-Oligocene Climate Transition: Reconstructions from Fluvial Strata of the White River Group, Toadstool Geologic Park, Nebraska

Anjali M. Fernandes[1], Michael T Hren[2], Jr., Queenie Chang[1], Virginia B. Smith[3], Baylee McGinnis[2], Dennis O. Terry, Jr.[4], David B. Luffman[1], Mia M. Rhodes[1], Yvette Eley[2], Madelyn A. Kurtz[1], Sarah E. Heithaus[1]

[1] Department of Earth and Environmental Sciences, Denison University, 100 W College St.,Granville, OH 43023

[2] Department of Earth Sciences, University of Connecticut, 354 Mansfield Rd,Unit 1045, Storrs, CT 06269

[3] Department of Civil and Environmental Engineering, Villanova University, 800 Lancaster Ave., Villanova, PA 19085

[4] Department of Earth & Environmental Science, Temple University, Philadelphia, PA 19122

Corresponding author: Anjali M. Fernandes (fernandesa@denison.edu)

Abstract

The Early Oligocene was a pivotal time in Earth's history. It marked the beginning of the Eocene-Oligocene Transition, when the earth's climate started shifting from a warm, greenhouse state to a cooler, drier icehouse state. During this transition, global sea surface temperatures dropped by about 6°C, and the first permanent ice sheets formed in Antarctica.

In North America, particularly in the modern Great Plains, landscapes were relatively tectonically stable following the end of the Laramide uplift. However, this period may have brought enhanced seasonality, colder winters, and fluctuations in volcanogenic sediment supplied by the Great Basin eruptions. Despite many studies on climate change, tectonics, and volcanism from this era, the specifics of rivers, floodplains, and catchments remain underexplored.

To fill this gap, we conducted a detailed study of early Oligocene river systems in the Orella Member of the Brule Formation of the White River Group at Toadstool Geologic Park in Nebraska. Our approach combined descriptive and quantitative methods to reconstruct river flow, sediment transport, channel dynamics, floodplain behavior, and catchment-scale moisture variability and ecosystem function.

We found that rivers were ephemeral, with peak flow depths and widths of approximately 2.5 m and 65 m respectively. Median peak discharges were approximately 168 cms, and base flows near zero, as indicated by subaerial exposure surfaces on river beds. Floodplains were dynamic and built by frequent floods able to suspend and deposit sand up to 200 microns, with relatively short intervening periods of stasis for soil development. Environmental information recorded in *n*-alkane δD, $\delta^{13}C$, average chain lengths (ACL) was similar and primarily inherited from transported plant material. The paleo-catchment relief, estimated from variability in δD values and modern altitude-driven lapse rates, was approximately 800 meters. River channels had a gradient of approximately 3×10^{-4}, an order of magnitude less steep than modern rivers in the area. This difference is likely due to the eastward tilting of the Great Plains

associated with dynamic topography that initiated during the Miocene. Modern river discharges are an order of magnitude lower and current mean annual precipitation is 100 - 220 mm less than during early Oligocene time; together, these estimates indicate greater moisture availability on early Oligocene landscapes relative to today, possibly due to lower paleo-landscape elevations at the time.

Our study provides a detail-rich characterization of Early Oligocene landscapes in Nebraska, offering insights into the hydrology, morphology, paleo-elevation, and relief of rivers and catchments during this period. The coordinated approach we used integrates hydroclimatic reconstructions, river and floodplain dynamics, and sediment and water fluxes, thereby bridging the timescale gap between geological records and modern hydrological data and ensuring consistency in reconstructions across subdisciplines. Our approach can support improved predictive modeling of paired climate-river dynamics through time.

1 Introduction

Earth's deep-time sedimentary and biogeochemical archive is a valuable and under-utilized dataset with which the coupling between climate, ecosystem and river dynamics can be studied, without accounting for anthropogenic modifications to landscapes. A look back at our planet's geologic past before humans existed - specifically the record of water availability on ancient landscapes, and the routing of sediment and water through them - can help us refine predictive models and prepare society for future change. Comprehensive hindcasts of climatic conditions (e.g., temperature, moisture availability) linked to river landscape characteristics (e.g., sediment fluxes, water fluxes, discharge variability) are a valuable foundation for informing and calibrating models that forecast landscape change on multi-generational timescales.

Here we generate an integrated characterization of Early Oligocene catchments and rivers from fluvial strata of the Orella Member (OM) of the Brule Formation of the White River Group (WRG) exposed at Toadstool Geologic Park (TGP), Nebraska, U. S. A.. The studied strata record characteristics of river landscapes from a period of heightened seasonality at the onset of the long term global climate transition from an Eocene greenhouse state to an icehouse state ((Zachos et al., 2001; Wade et al., 2012). We use the physical characteristics of river and floodplain strata to reconstruct paleo-hydraulic and sediment transport characteristics of rivers, and the chemical signatures of moisture availability encoded in leaf waxes of ancient plants in river and floodplain sediment to reconstruct hydroclimatic variability and relief across paleo-catchments. We compare reconstructions of paleo-catchments and -rivers to modern fluvial systems, and assess how climate, topography and the routing of sediment and water has changed since the Early Oligocene.

With this work, we advance the state of knowledge in two ways. First, we generate a detail-rich characterization of fluvial landscapes in northwestern Nebraska, U. S. A., at the beginning of the Eocene Oligocene Transition (EOT) when the Earth's climate had begun the transition from a greenhouse to an icehouse state. Our approach quantifies properties of paleo-rivers and catchments at a range of temporal and spatial scales, from minutes and hours associated with flooding ephemeral streams, to channel hydraulic geometry adjustment on centennial or millennial timescales, to local or regionally integrated signals of climate that span 10^4 - 10^5 years or more. Second, we develop a workflow that integrates methods and data that have historically been generated in isolation and can sometimes present conflicting results.

Such paired climate-and-river reconstructions are particularly powerful because they: (1) deliver estimates of flow and sediment transport on temporal and spatial scales that are compatible with predictive hydraulic and sediment transport modeling tools (e.g., Fathi et al., in review, Water Resources Research), (2) can be used to test for internal consistency between reconstructions of river hydraulics and morphodynamics from the sedimentary record and reconstructions of hydroclimate and catchment relief from the biogeochemical archive, and (3) bridge the timescale gap between hindcasts from the geologic record, modern hydrological data with hourly to decadal resolution and model forecasts generated on hourly to millennial time-scales.

1.1. Background: The Early Oligocene in North America

1.1.1. Climate

The early Oligocene was a pivotal period in Earth's history. Following the early Eocene thermal maximum from 53-50 Ma (Miller et al.), global climates cooled from the greenhouse climate of the late Mesozoic and early Paleogene to the icehouse climate of the late Paleogene and Recent (Fischer, 1982). This cooling trend began during the EOT (33.9 - 33.5 Ma) and is marked by extensive perturbations in global climate superimposed on a long-term phase of cooling and drying (Zachos et al., 2001). Marine records of this transition are marked by dramatic shifts in carbon and oxygen isotopes near the Eocene-Oligocene boundary, the extinction of microfossil lineages, and the appearance of permanent glacial conditions on Antarctica (e.g. (Ivany et al., 2003, 2006; Galeotti et al., 2016).

Beginning at ~33.9 Ma, for a period of ~300,000 years, atmospheric carbon dioxide (CO_2) concentrations fluctuated between highs of ~1,100 p.p.m.v. to below 750 p.p.m.v. and produced variability in atmospheric and oceanic circulation patterns (Zachos et al., 2001). In combination with favorable orbital parameters such as insolation minima, atmospheric pCO_2 ultimately crossed a threshold which resulted in the establishment of the first large-scale permanent ice sheets on Antarctica (Ivany et al., 2003, 2006; Galeotti et al., 2016). Marine isotope records indicate a ~6 ^{o}C decrease in global sea surface temperature (Coxall et al., 2005). Planktic foraminifera $\delta^{18}O$ are interpreted to reflect enhanced seasonality in the Gulf of Mexico from 33.7 Ma onwards, marked by increasingly cold winters (Wade et al., 2012). Unlike the marine archive, however, terrestrial records of climatic change during the EOT are sparse, and highly variable (Lauretano et al., 2021).

Climate model projections for western North America suggest that the reduced pCO_2 would have likely lowered temperatures and reduced precipitation (Poulsen and Louise Jeffery, 2011). However, while North American terrestrial records indicate a cooling pattern, estimates of temperature change are highly variable, i.e., they range from <2 °C to 8 °C (Zanazzi et al., 2007; Retallack, 2007; Sheldon, 2009). Chemical indices of alteration and soil carbonates from paleosols suggest a decrease in mean annual precipitation (MAP) across the EOT (Sheldon and Retallack, 2004). Stable isotope data from fossil bones and teeth found in the White River Group indicate an estimated 7 °C decrease in temperature (Zanazzi et al., 2007; Retallack, 2007; Sheldon, 2009); Fig. 1A). Surprisingly, this change does not accompany any estimated change in water availability or the oxygen isotopic composition of precipitation (Zanazzi et al., 2007; Retallack, 2007; Sheldon, 2009)).

From WRG strata that span the EOT at TGP, (Terry et al., 2001) estimated that mean annual precipitation (MAP) shifted from ~855mm in the Late Eocene to ~739 mm. (Terry et al., 2001) also inferred a transition from humid forests of the late Eocene to seasonally wet, semi arid savannas in the early Oligocene with evidence of abundant plant life recorded by hairline root structures similar to modern mollic epipedons of prairie soils (i.e., mollisols). He noted that weakly developed soils - inceptisols - in early Oligocene floodplain strata suggested a cool, dry climate. At Douglas, WY, U. S. A., (Retallack, 2007) estimated a MAP of 652-628 mm from Early Oligocene strata. From the Badlands of South Dakota, (Retallack, 1992) estimated a decrease in MAP from >1000 mm in the Eocene to 500-900 mm in the Early Oligocene. Here, we integrate existing plaeo-climatic reconstructions with paleo-hydraulic reconstructions of Oligocene rivers to generate a characterization of moisture availability and river dynamics on Early Oligocene terrestrial landscapes in Nebraska, U. S. A.

1.1.2. Tectonic Change

The Early Oligocene interval in question is thought to post-date significant uplift in the North American Cordillera (~40 - 38 Ma) associated with the Laramide orogeny (DeCelles, 2004; Mix et al., 2011; Chamberlain et al., 2012; Fan et al., 2018). The Laramide orogeny occurred because of compression during the shallow subduction of the oceanic Farallon plate beneath the North American continental plate (DeCelles, 2004). Post-Laramide extensional tectonics, associated with the roll-back or sink of the subducting slab and the consequent upwelling of asthenospheric upper mantle from north to south (Humphreys, 1995; Schmandt and Humphreys, 2010), created a rapidly propagating north-to-south wave of surface uplift. By the early Eocene (~ 50 Ma), a topographic wave had developed in northwestern North America (British Columbia and eastern Washington); the wave of topographic relief then swept southward, reaching mid-western North America (northeastern Nevada) by ~40 to 38 Ma and shifting further into southern Nevada by ~23 Ma (Chamberlain et al., 2012).

The mean elevation and the relief between the central Rockies and the western Great Plains is thought to have reached present-day levels during the late Eocene (Sjostrom et al., 2006; Mix et al., 2011; Chamberlain et al., 2012; Fan et al., 2014a, 2014b). The surface uplift of the central Rockies at this time is expressed through a widespread disconformity spanning ~42-37 Ma, between the upper Cretaceous and the late Eocene strata in western Nebraska (Cather et al., 2012) and the supply of coarse-grained sediment to fluvial systems on the Great Plains since then (Galloway et al., 2011; Blum et al., 2017).

1.1.3. Orogenic Influences on Moisture Transport

Moderate uplift in the southern North American Cordillera during the late Eocene has been linked to aridification of central North America due to the development of a regional orographic rain shadow (Fan et al., 2014a, 2020). During this period, the likely sources of moisture in the region were the Gulf of Mexico and the Pacific Ocean. However, the ~4 km Sevier hinterland during the Eocene and beyond (Chamberlain et al., 2012) is likely to have limited the potential for significant inputs of precipitation from the Pacific Ocean (Fan et al., 2018).

Regional drying, reflected in a time-transgressive wave of loess deposition that started at approximately 36 Ma in the central Rockies and expanded eastward to the Great Plains, occurred across the ~33.9 Ma onset of the EOT. The effect of the rainshadow is thought to have been enhanced by the cooling and drying of regional and global climate during the EOT. In western Nebraska, the region studied here, significant loess deposition began at ~31.6 Ma, well after the start of the EOT, and is marked by the boundary between the OM and the overlying Whitney Member of the Brule Formation of the WRG (Fig. 1C). Here, we focus on characteristics of the fluvial strata of the Early Oligocene Orella Member which predates significant eolian deposition in this region.

1.1.4. Post-orogenic Uplift of the Great Plains

Various authors have argued for post-Laramide (i.e., after ~40 Ma) rejuvenation of the Rocky Mountain Orogenic Plateau and dynamic topography-driven eastward tilting along the western Great Plains during the Late Cenozoic, e.g., (Heller et al., 2003; Fernandes and Roberts, 2021). Lines of evidence in support of geologically recent rejuvenation of the Colorado Front Range and Great Plains include: a) reconstructions of paleo-river gradients and stratal geometries (McMillan et al., 2002, 2006; Leonard, 2002; Heller et al., 2003; Duller et al., 2012; Marder et al., 2024) that imply temporally steepening river long profiles, b) seismic and topographic data and mantle convection models (Moucha et al., 2008, 2009; Karlstrom et al., 2012; Hansen et al., 2013; Rosenberg et al., 2014) that suggest unusually warm, low-velocity zones in the mantle beneath the Colorado Front Range, c) thermochronology from the Southern Rockies that indicates geologically recent differential uplift and active tectonism (Abbey et al., 2018; Abbey and Niemi, 2018), d) paleo-altimetric and -biological reconstructions that support a west-to-east decrease in uplift rates along the Colorado Front Range (Fernandes and Roberts, 2021), and e) numerical models that link subduction dynamics, mantle flow and patterns of epeirogenic uplift to predict enhanced exhumation and incision rates downstream along the Colorado Front Range (Mitrovica et al., 1989; Tucker and van der Beek, 2013). Here, we add early Oligocene river profile reconstructions to the temporal record of river long profiles in the Great Plains Region.

1.1.5. Volcanism

Early Oligocene landscapes in North America may have been influenced by intermittent volcanogenic alterations in the sediment fluxes of rivers. Geochemistry of mineral phases and age correlation of volcanic tuffs indicate that Great Basin volcanism was a major source of tuffaceous sediment in the Eocene - Oligocene WRG strata (Larson and Evanoff, 1998). Pyroclastic volcanism in the Great Basin (~36 Ma) region (Larson and Evanoff, 1998; Best et al., 2009, 2013) is linked to the roll-back of the Farallon plate during subduction from the late Eocene to Oligocene (Sato and Denson, 1967; Lipman and McIntosh, 2008; Best et al., 2009, 2013). Explosive volcanism and ignimbrite flareups in eastern Nevada and western Utah were active from ~36 Ma - 18 Ma (Best et al., 2009, 2013). Thus, temporally unstable sediment fluxes, linked to volcanogenic sediment influx, may have influenced the dynamics and sedimentation of the rivers explored here.

A significant body of research has focused on climate, topography and volcanism in N. America during this period in Earth history (e.g., (Sjostrom et al., 2006; Zanazzi et al., 2007; Boardman and Secord, 2013; Fan et al., 2020). However, with few notable exceptions (Korus and Joeckel), the characteristics of paleo-rivers, -floodplains and -catchments of this time are relatively under-constrained. Here, we address this knowledge gap with a complementary, coordinated approach to reconstruct river landscapes during the Early Oligocene. Our purpose with this work is to focus on the sedimentary record of North American fluvial landscapes preserved within the Early Oligocene Orella Member of the Brule Formation of the White River Group in Nebraska, U. S. A, between ~33.9 Ma and ~ 33.4 Ma, a key interval that is contemporaneous with the onset of the EOT.

1.2. Study area

The WRG in Nebraska is an extensive terrestrial sequence that spans the EOT in western North America; however, the TGP sequence is - to our knowledge - unique in that it provides a thick, well-dated, terrestrial sequence that can be temporally linked to the onset of the long term shift in global climate (Grandstaff and Terry, 2009; Sahy et al., 2015). WRG depositional environments include fluvial, lacustrine and eolian deposits that incorporate fine-grained reworked volcanic sediments and detrital siliciclastic sediment derived from the Hartville, Laramie and Black Hills uplifts (Terry et al., 2001; Grandstaff and Terry, 2009; Sahy et al., 2015). Here, we use the age control framework provided by Sahy et al. (2015), which is revised and updated from magnetostratigraphy (Prothero and Emry, 1996), supplemented with tephrostratigraphic correlations and $^{206}Pb/^{238}U$ zircon dates from 6 volcanic tuffs (Sahy et al., 2015). Sahy et al. (2015) report uncertainty on these $^{206}Pb/^{238}U$ zircon dates in the order of 100,000 – 150,000 years.

We mapped outcrops of the Orella Member of the Brule Formation of the White River Group (WRG), Toadstool Geologic Park (TGP), outside Crawford, Nebraska, U. S. A. (Fig. 1D -I).The Oligocene Brule Formation conformably overlies the late Eocene Chadron Formation elsewhere in the section; but is associated with local erosion and removal of up to 10 m of thickness of the Chadron Formation through the studied interval at TGP (Grandstaff and Terry, 2009; Sahy et al., 2015).

1.2.1 The Orella Member of the Brule Formation, White River Group: Toadstool Geologic Park, Nebraska, U. S. A.

The exposures of the Orella Member (OM) within TGP are laterally extensive and approximately 50-m-thick (Sahy et al., 2015). They are primarily composed of pale, interbedded sheet sandstone and volcaniclastic claystone and siltstone. The outcrop belt exhibits steep hillslopes of pale, weakly cemented mudstones, dissected by drainage channels, and thinly to thickly bedded cliff- and bench-forming sandstones. Weathering and erosion of thin- to medium-bedded sandstones overlying mudstones have created an interesting toadstool-like expression, for which the park is named, on hillsides formed by these strata.

Looking west from the TGP campground parking lot (Fig. 1 H-I), the boundary between the Early Oligocene OM and the underlying late Eocene Big Cottonwood Creek Member is clearly marked by the Upper Purplish White (UPW) ash layer dated at 33. 9 Ma (Schultz and Stout, 1955; Sahy et al., 2015). This ash layer is gray to the naked eye. The UPW layer was first described and named by scientists wearing purple-tinted sunglasses as protection against the intense glare off the pale strata.

The lowermost OM strata above the UPW comprise recurrent thinly bedded sandstone sheets interbedded with siltstones; these strata are several meters thick at some locations but have been removed by erosion associated with an unconformity elsewhere (Grandstaff and Terry, 2009; Sahy et al., 2015. Two erosionally-based, multistoried sandstone bodies, separated by laminated mudstones, overlie the unconformity. Here, we identify them as the lower sand body and the upper sand body (Fig. 1 H-I). They are dominated by inclined sets of north-eastward dipping, upward-fining, very fine-grained to coarse-grained, thinly- to thickly bedded, trough cross-stratified, sub- to super-critically climbing ripple laminated, plane laminated or structureless sandstone beds (Fig. 1H, Fig. 2, Fig. S1). Exposed tops of inclined beds are traceable horizontally for 10s of meters (Fig. 2A-B; Fig. S1). The surfaces of sandstone beds are commonly marked by mudcracks (Fig. 2E), burrows (Fig. 2I) and well-preserved mammal hoofprints superimposed on ripple crests (Fig. 2C, 2D); abundant, mud-rich climbing ripple laminated deposits and climbing dune cross-stratified deposits are commonly associated with soft sediment deformation features (Fig. 2F, G, H). The sand bodies are encased in fine-grained horizontally bedded mudstones with recurrent, closely spaced, ledge-forming tabular sandstone or siltstone beds.

Above the upper sand body and below the Serendipity Ash (dated 33.414 +/- 0.035 Ma, Fig. 1H-I; Fig. S2; (Sahy et al., 2015), the outcrop is dominated by brown to orange, volcaniclastic claystone to siltstone interbedded with pale-brown tabular sandstones (Fig. 1H-I, Fig. S14). Paleosols mapped through this section were described by Terry et al. (2001), as weakly developed inceptisols. Tabular sandstones are thin to medium-bedded (less than 0.2 m thick), fine-to-medium-grained, plane- or ripple-laminated and rarely cross-bedded. Multiple erosional features, some of which are draped by volcanic ash (Fig.S-2), truncate horizontally bedded sheet sandstones and siltstones. Sedimentation within and overlying erosional features is mud-dominated, horizontally bedded, with repetitive flat-lying sandstone and siltstone beds and rare erosionally-based, inclined sets of sandstone beds. Weakly developed reddish-brown or orange paleosols are common.

Above the Serendipity ash and to the boundary between the OM and the overlying contact with the Whitney Member, the outcrop is dominated by silty mudstone and interbedded tabular sandstones that are pedogenically modified and fine upward (Lukens, 2013). No erosional features on the scale observed lower in the stratigraphy are seen here.

1.2.2. A General Paleoenvironmental Interpretation to Support Field Sampling Protocols for Paleohydraulic Reconstructions

This sequence was previously described as the TGP channel complex (Schultz and Stout, 1955; LaGarry, 1998). The inclined sandstone beds are interpreted as channel bar deposits and adjacent flat-lying interbedded sandstones and mudstones as overbank floodplain deposits. When individual inclined beds thin upwards and flatten out as they transition into finer grained mudstones and siltstones of adjacent floodplains, they are interpreted as fully-preserved channel bars. Truncated by the channel sandstones, recurrent tabular sandstones interbedded with thinly laminated claystone and siltstone are interpreted as crevasse splay deposits on floodplains. The erosional features above the upper sandstone body and below the Serendipity Ash are interpreted to be the result of periods of sustained channel incision.

Within the channel sand bodies, abundant dune cross stratification and plane lamination indicate high transport stages. Climbing ripples, climbing dunes and soft sediment deformation indicate rapid suspended sediment deposition. High suspended sediment loads are indicated by the significant volumes of mud present in the bed material load and the abundant sedimentary structures associated with deposition from suspension. Mudcracks and mammal hoof prints on the channel beds (Fig. 2C-E) suggest that subaerial exposure of channel beds between high flow events was common.

2. Materials and Methods

2.1. Fieldwork Protocols for Characterizing Early Oligocene Deposits

Outcrop data collection was coordinated around paired landscape and climate reconstructions of rivers and their catchments. We collected high-resolution ground-based LiDAR with a Leica 360 RTC lidar scanner. The LiDAR was processed with aid from the NEHR Natural Hazards Reconnaissance facility using Cloud Compare and made available for analysis through ArcGIS and Potree. The LiDAR scans (Table S-1) were used for measurements of height and length in situations where outcrop access was challenging or when a “birds-eye” view was necessary for mapping features in three dimensions. Locations that were difficult to access and to shoot with the LiDAR unit were photographed at high resolution, and key elevations measured with a laser range finder.

We generated vertical stratigraphic columns to characterize bed thicknesses, sand body thicknesses and sedimentary facies (Fig. 2J). We coupled these with detailed horizontal maps of sedimentary structures on exhumed bar deposits and their transition into floodplain deposits wherever possible. Paleocurrent directions, measured from exposed ripple crests, flow lineations, exposed dunes, trough cross-beds and flute casts in bar strata were recorded as was the direction of dip of the bar surfaces (Figure S-1).

Field measurements, LiDAR data and scaled photographs were used to measure: 1) dimensions of 110 bar clinoforms (Fig. 3A-B; Fig. S3; Table S-2, 2) thicknesses of 125 dune cross-sets (Table S-3), 3) angles of climb on 48 sets of climbing ripple sets and climbing dune cross-sets (Table S-4), and 4) the relief on observed erosional surfaces (Fig. S-2).

We collected 101 georeferenced rock samples that were keyed to sedimentary facies and to interpreted position on the paleo-landscape, i.e., channel or floodplain, for paired geochemical and sedimentological analyses. To link detailed grain-size distributions of deposits to different transport modes, we sampled deposits associated with (a) channel bed material load (n=35), which included plane-laminated, cross-stratified and ripple-laminated sandstones, and (b) channel suspended load and washload (n=39), which included climbing ripple laminated and climbing dune stratified sandstones, in-channel mud-rich sediment drapes or mud deposits at the toes of inclined bar strata, and (d) laminated, rippled or structureless floodplain sandstones and mudstones (n=27). Detailed grain-size distributions were extracted from all 101 samples. The geochemical analyses, used for estimates of paleo-catchment relief and variability in moisture availability, are more time-consuming and expensive and were applied to 9 channel deposit samples and 6 floodplain deposit samples.

2.2. Reconstructing Paleohydraulic and Sediment Transport Patterns in early Oligocene Rivers

2.2.1. Quantitative Constraints on River Flow and Sediment Transport

<u>*2.2.1.1. Channel Width, Depth and Longitudinal Slope*</u>

We used fully-preserved bars (n=6), as proxies for bank full flow depth (H_{bf};(Mohrig et al., 2000; Chamberlin and Hajek, 2019); truncated and partially preserved bars were used as proxies for minimum flow depth (H_{min}; n=104). On exposures that were transverse to flow, we used the measured widths of fully-preserved bar clinoforms (W_{bar_full}) to estimate bank full flow width (B_{bf}); truncated/partially preserved bar clinoforms were used as estimates of minimum flow width (Fig. 1J - K) using the empirical relationship established by (Greenberg et al., 2021):

$$B_{bf} = (2.34 \pm 0.13)W_{bar\_full} \quad \text{(Eq. 1)}$$

We used detailed grain-size data from bed material load samples (See Supplementary Information S-1 for detailed lab methods for grain-size extraction). Based on the relationships developed by (Trampush et al., 2014) and (Mahon and McElroy, 2018), we estimated paleoslope, S, using median particle diameter D50 of bed material and estimates of channel depth Hbf:

$$\log S = a_0 + a_1 * \log D_{50} + a_2 * \log H_{bf} \quad \text{(Eq. 2)}$$

Where $a_0 = -2.08$, $a_1 = 0.254$, and $a_2 = -1.09$ are empirical coefficients.

2.2.1.2. Peak Flow

We implemented the (Bagnold, 1966) assumption that the shear velocity (u_*) of a transporting flow must be quasi-equal to the settling velocity (w_s; estimated after Dietrich (1982)) of the D_{95} of fully-suspended sediment sampled from climbing ripples and dunes. Using a drag coefficient $C_D = 0.21$ appropriate for sand bedded rivers (Lynds et al., 2014), we estimated the depth-averaged water velocity at peak flow (U_{avg})

$$U_{avg} = u* / C_D \quad \text{(Eq. 3)}$$

By assuming that sediment trapped in climbing bedforms was deposited in the period subsequent to peak flood, we generated estimates of peak water flux (Q_{w_bf}) using depth averaged velocity U_{avg} and the width (B_{bf}) and depth (H_{bf}) of bank full flow

$$Q_{w\_bf} = U_{avg} * B_{bf} * H_{bf} \quad \text{(Eq. 4)}$$

2.2.1.2. Bedload Flux and Height of Formative Bedforms

We used the relationships developed by Mahon and McElroy, 2018, to estimate dune translation rate (V_x) and unit bedload flux (Q_{bed}) as shown below:

$$\log V_x = b_0 + b_1 * \text{Log } S \qquad \text{(Eq. 5)}$$

Where $b_0 = 0.6113$, $b_1 = 1.305$ are empirical coefficients,

$$Q_{bed} = \varepsilon_{bed} * H_{bf} * V_x / 2 \qquad \text{(Eq. 6)}$$

Where ε_{bed} is the concentration of sediment in the bed and is given by 1- porosity, where porosity is estimated to be 35%.

We measured the thickness of 125 cross-sets in the field or from scaled field photographs (Fig. 3G, Table S-3). Only cross-sets that did not display identifiable internal stratification associated with bars or compound bedforms were used in these measurements. Cross-set thicknesses (H_{st}) were then used to generate distributions of estimated bedform heights (H_{bed}), using the relationships developed by (Das et al., 2022).

$$\mathbf{H_{bed} = (2.9 +/- 0.7\ ) * H_{st}} \qquad \text{(Eq. 7)}$$

2.2.1.4. Minimum duration of depositional events

Using the climb angles (ς) on climbing ripples and dunes, together with the downstream translation rates (V_x) from Eq. 5, we estimated the vertical translation rate or aggradation rate of the sediment bed (Allen, 1970, 1971; Rubin and Hunter, 1982).

$$V_z = 2 (\tan \varsigma) V_x \qquad \text{(Eq. 8)}$$

Accounting for sediment concentration in the bed, we estimated deposition rate (R_D)

$$R_D = V_z \, \varepsilon_{bed} \qquad \text{(Eq. 9)}$$

Using the thicknesses of the units displaying climbing ripples or climbing dunes measured in the field or from scaled photographs, we estimated the minimum duration of depositional events associated with the falling limbs of floods. In beds where climbing bedform lamination/stratification only represented a fraction of the bed thickness, the full duration of the depositional phase of the flood could not be estimated (Allen, 1971).

$$T_{deposition} = H_{layer} / R_D \qquad \text{(Eq. 10)}$$

2.3. Quantitative Constraints on Catchment Relief

We used cuticular plant waxes, *n*-alkanes, in organic matter preserved in 9 channel deposit samples and 6 floodplain samples to characterize moisture availability and the scale of catchment relief. *n*-alkanes are waxes produced on the surface of plant leaves to aid in water repellency and shield against moisture loss (Holloway, 1969; Neinhuis and Barthlott, 1997). They can be preserved over long timescales (Schimmelmann et al., 1997; Yang et al., 2011) and with minimal isotopic alteration. The details of laboratory methods used for geochemical analyses are provided in Section S-2 of the supplementary information file.

Organic matter found in fluvial deposits can originate from two sources: detrital material, which carries environmental information integrated from the entire catchment area, or in situ deposits from local vegetation, which reflect local environmental conditions. If the organic matter is catchment-integrated, the environmental signals may span $>10^5$ years and encompass large spatial areas corresponding to the size of the catchment. In contrast, locally sourced organic matter may capture environmental signals over years to thousands of years, representing much smaller spatial scales. (Fernandes et al.; Chang et al., 2023)

In young floodplain surfaces or channels, the organic carbon is mainly detrital, derived from various parts of the upstream catchment area. Conversely, mature floodplain surfaces, which remain stable long enough to develop soils, accumulate significant amounts of in situ organic carbon that contains local environmental signals (Bobik, 2021). Therefore, analyzing channel and floodplain dynamics through their sedimentary records provides valuable context for understanding the scale of integration in terrestrial paleoclimate reconstructions from organic carbon, and for recovering paleoenvironmental information from other parts of the catchment.

We based our reconstructions on 3 proxies of environmental state:

(2) Distributions of δD in plant lipids: The hydrogen isotopes of modern cuticular waxes reflect a time-averaged record of the δD of precipitation, water availability in the environment, and biological fractionation occurring during lipid synthesis (Sachse et al., 2012). Precipitation δD is primarily controlled by the isotopic composition of source moisture, the temperature of condensation, moisture transport path and distillation processes (Gat, 1996).

In the Great Plains, modern precipitation is derived from the Pacific Ocean and the Gulf of Mexico (Fig. 1D). Moisture originating from the Gulf of Mexico today is ~30‰ enriched in deuterium compared to moisture from colder Pacific and/or polar regions (Liu et al., 2013). Seasonal variations in temperature in these regions can alter the isotope composition of air masses that bring moisture from the Pacific Ocean and Gulf of Mexico to the Great Plains.

Limited significant inputs of isotopically negative precipitation from the Pacific Ocean is expected during the Eocene and beyond owing to the ~4 km Sevier hinterland (Fan and Dettman, 2009;

Chamberlain et al., 2012; Fan et al., 2018). (Fan et al., 2014a) showed that δD values of water recovered from volcanic glasses from the Eocene through Miocene and calculated surface water δD display an eastward increase and lapse rate of 5‰ - 11‰ per degree longitude, similar to modern day values calculated from the $\delta^{18}O$ of precipitation.

To quantify paleo-catchment relief, we used the δD of modern river water across the Great Plains (Kendall and Coplen, 2001). The isotope composition of river water integrates the temporal and spatial variability of the local hydrological cycle over the scale of the drainage basin (Kendall and Coplen, 2001)). This means that rivers can capture the overall groundwater/recharge isotope signal of a region more comprehensively than a single rainfall event (Kendall and Coplen, 2001). We only selected data points from rivers with small drainage areas (<20,000Km2), to minimize potential biases related to varied catchment hypsometry (Table S-5). This modern dataset also inherently includes heterogeneity in the proportion of moisture from the Gulf of Mexico and the Pacific Ocean (Kendall and Coplen, 2001). Mean δD of modern river water shows an eastward increase with a lapse rate of 7.6 ‰ per degree longitude, a similar value to the 5‰ - 11‰ per degree longitude estimated lapse rates from Eocene through modern estimates (Fan et al., 2014a). We assumed that altitude-driven δD lapse rates during the Oligocene were similar to that seen today and we estimated catchment relief using an estimated lapse rate for modern drainage basins in the Great Plains. To do this, we assumed the maximum and minimum δD values recovered from ancient cuticular waxes were proxies for the potential range in catchment elevation.

(2) $\delta^{13}C$ of plants and their biomarkers: The carbon isotope composition of C_3 plants reflect ambient precipitation amount and physiological responses to moisture deficit or atmospheric pCO_2 (e.g., (Diefendorf et al., 2010). $\delta^{13}C$ in plant tissue reflects the pathway of carbon fixation, overprinted by environmental stresses such as water availability. When subjected to water stress, the stomatal conductance of C_3 plants decreases to maintain water use efficiency, resulting in a positive shift in the carbon isotope composition of plant tissue (Farquhar et al., 1989). Lower temperatures, on the other hand, produce more negative $\delta^{13}C$ values. We used the range in $\delta^{13}C$ values from organic matter as a proxy for variability in plant physiology that may occur due to variability in moisture availability and temperature at different altitudes within a drainage basin.

(3) Distributions of n-alkanes (Average Chain Length, ACL): Plants in biomes with reduced atmospheric moisture typically have larger ACL values than plants growing in wetter habitats (Bush and McInerney, 2013). Eley and Hren (2018) provided a relationship between ecosystem-averaged ACL values and vapor pressure deficit, across varying vegetation distributions and climates. ACL distributions can change dramatically as a function of environmental conditions and correlates well with atmospheric vapor pressure deficit (Eley and Hren, 2018). We used the range in ACL values in n-alkanes as a measure of variability in moisture availability across the drainage basins associated with the studied strata.

2.4. A Survey Dataset of Modern Great Plains Rivers and Catchments

We characterized the hydrology of six streams in the Great Plains—the North Loup, Niobrara, Calamus, Platte, Republican, and Ninnescah—using data from 23 United States Geological Survey (USGS) streamflow gauges (Fig. 4A, Table S-6). Using stream maps from Elevation Derivatives for National Applications (EDNA) provided by the USGS, we measured the mean longitudinal slopes of the rivers (Fig. 4B) along the longest channel path from the highest elevation headwater to the relevant stream gauge, using Google Earth. Also with EDNA stream maps, we manually delineated the drainage basins for each gauge in Google Earth using the polygon tool (Fig. 4A) and measured the drainage area (Fig. S4). The catchment shape files, exported from Google Earth and loaded into ArcGIS, were combined with a 30-meter regional DEM to generate elevation distributions for each catchment (Fig. S4) and estimates of catchment relief (Fig 4E).

We averaged yearly rainfall data from meteorological stations across each catchment to determine the mean annual precipitation for the area drained by each gauge (Fig. 4C).We compiled modern discharge distributions from continuous discharge series, with measurements taken at 0.25 to 1-hour intervals, from the 23 USGS streamflow gauges (Fig. 4D; Table S-6). Gauges within watersheds that had undergone significant engineered modifications, such as reservoirs, were either excluded from the dataset or the data was limited to periods before such modifications occurred. These data do not, however, account for alterations to groundwater discharge or land-use patterns that may impact stream-flow measurements.

3. Results, Interpretation and Implications

3.1. Descriptive and Quantitative Characterization of Early Oligocene Fluvial Strata at Toadstool Geologic Park, NE

The measured thickness of the lower OM channel sand body is 5 - 6m. whereas estimated peak flow depths from fully preserved barforms was 1.6 - 2.8 m (Fig. 2J, Table S2). Estimated flow width at peak flow was 56 +/- 3 m. The estimated ratio of sand body thickness to bank full flow depth is 2 - 3. The thickest fully preserved bar clinoforms were recorded at the top of the sand body. We interpret that these fully preserved bars formed during a period just prior to abandonment and that overlying fine grained strata associated with abandonment preserved the full clinoform thickness. By contrast, fully preserved bar clinoforms lower in the section are thinner by more than a meter, while truncated bar clinoforms are as thick as 1.9 m. As smaller barforms are most likely to be preserved during channel migration, we infer that bank full flow depth estimates from lower levels in this sand body may be biased towards smaller values.

The lower OM sand body overlies an unconformity that is associated with removal of up to 10m of the underlying Big Cottonwood Creek Formation (Sahy et al., 2015). Although discontinuous outcrops of the lower OM sand body could be mapped for ~400m, bar clinoforms were not traceable over significant horizontal distances. (Mohrig et al., 2000) demonstrated that freely avulsing, i.e., unconfined, river systems can grade to roughly 1.6 times bank full flow depths before the channel is primed to avulse; the resulting sand body is thus expected to be roughly 1.6 times the bank full flow depth. We infer that the lower sand body was the product of deposition within a channel confined to an erosional corridor that was at least 6.5 m deep and that erosional relief exceeded peak flow depths. It is likely that the erosional relief prevented channel avulsion and facilitated the construction of a sand body that is significantly thicker than estimated flow depth ((Mohrig et al., 2000). We infer that the larger sand body thickness measurements correlate with locations closer to the axis of the erosional corridor, while smaller thickness measurements are associated with the lateral margins.

The upper sand body is ~4m thick and is separated from the lower sand body by ~2m of laminated claystone and siltstone. Estimated peak flow depths and widths are 2.3 - 4.4 m and 70 +/- 4m, respectively. The sand body is therefore 1-1.5 times the estimated bank full flow depth (Fig. 3C), Individual bar deposits in the upper sand body could be mapped horizontally for tens of meters (Fig. 2A-B; Fig. S-1). **Based on the ratio of sand body thickness to flow depth, we infer that the upper sand body was created by a channel that was free to migrate and avulse laterally, either outside of the filled-in, pre-existing erosional container that housed the lower sand body, or within a wider yet erosionally-confined floodplain. These estimates indicate an erosional relief that was at least 5m, but as much as 11m.**

We infer that limited lateral continuity of bar deposits in the lower sand body may have been due to significant internal erosion while laterally confined. By contrast, laterally continuous bar deposits in the upper sand body can be used to loosely reconstruct local channel planform. Across a ~5,000 sq. m horizontal exposure of the top of the upper channel sand body (Fig. 1H-I; Fig. 2A-B; Fig. S-1), bar clinoforms show dips towards ~N 80o at the southwestern extent of the outcrop that transition to ~N 60o at the northern extent of the outcrop. We infer that these strata preserve the record of **systematic north-eastward channel migration.**

Bar strata preserve a wide range of paleocurrent directions sometimes at high angles (>90º) to the dip directions of the bar surfaces but indicate an average southeasterly direction of transport (Fig. S-1). From the lateral continuity of bar clinoforms, systematic accretion patterns and evidence of complex flow patterns from sedimentary structures, we infer that the deposits were created by a sinuous channel with highly variable local bed topography (Fig. S-1). Exhumed three dimensional ~0.4 m scale bedforms, with curved lee faces that can be tracked along a ~180º arc (FIG. S-) and internal cross-stratification, near the bases of laterally continuous dipping clinoforms are interpreted as unit bars and/or free bars (Seminara and Tubino, 1989; Cardenas et al., 2020) that may be responsible for imparting some of the observed complexity in measured paleo-flow and -transport directions.

Bar clinoforms that intersect the horizontal surface are relatively straight along their exposed tops. Across the widest part of the outcrop (~46m in the cross-stream direction) bar clinoforms transition from a ~N 170º trend to ~N155º. We therefore infer that this outcrop preserves less than one channel width worth of lateral migration, and that the preserved strata are associated with a relatively small section of a bend characterized by a large radius of curvature and/or a high-amplitude bend.

Suspended load and washload channel deposits, including climbing ripple laminated, climbing dune stratified and structureless deposits, contained median particle sizes ranging from 10 μm to 200 μm (Fig. 3D). Using the 95th percentile of particle sizes in these deposits, we estimated a reasonable median depth-averaged peak flow velocity of 1.2 m/s (Fig. 3E) and median peak discharge of 168 m^3/s (Fig. 3F) (Bagnold, 1966; Dietrich, 1982; Lynds et al., 2014). Subaerial exposure of the Orella channel beds, evidenced by mudcracks and mammal hoof prints superimposed on ripples (Fig. 2D-E), support an inference that the formative channels were ephemeral and base flow was equal to or close to zero.

Bed material load deposits, from both channel sand bodies, with sedimentary structures linked to high transport stages and/or stages of waning transport, i.e. trough cross-stratified or plane-laminated sandstones, and sandstone beds with ripple reworked surfaces, contained median particle sizes ranging from 80 μm to 1000 μm (Fig. 3D). We estimated 3 x 10^{-4} to be the median reconstructed longitudinal gradient of formative channels (Fig. 3L) after (Trampush et al., 2014) and (Mahon and McElroy, 2018) and the estimated median downstream translation rate (i.e., celerity) of dunes is 10^{-5} m/s (Fig. 3M). These estimates fall between measurements for the modern Rio Parana (Santos and Stevaux, 2000), and the Calamus (Gabel, 1993), Waal (Kleinhans Maarten G. and Brinke Wilfried B. M. Ten, 2001) and North Loup (McElroy and Mohrig; Mohrig and Smith) (Fig. 3O), and are one or two orders of magnitude lower than experimental observations . The estimated early Oligocene median unit bedload flux is 4 x 10-5 (Fig. 3N) and similar to the North Loup (Fig. 3P).

The median of measured cross-set thicknesses (Fig. 3G; Table. S-3) is 0.1m. These measurements yielded an estimated median dune height of 0.2 - 0.4 m m (Fig. 3L; (Das et al., 2022)). Modern measurements from the North Loup (Mohrig, 1994), Calamus (Gabel, 1993), and Waal (Kleinhans Maarten G. and Brinke Wilfried B. M. Ten, 2001) are similar to our reconstructed values (Fig. 3H).

From significant volumes of mud in bed material load (~30%; Fig. 3D) and pervasive structures associated with suspension deposition, we infer that peak flow was accompanied by large, suspended sediment loads. Rapid deposition from suspension in low velocity zones and/or during waning floods is inferred from the abundance of closely associated climbing ripples, climbing dunes, and soft sediment deformation. From a distribution of measured climb angles (Fig. 3I, Table S4) we estimated a median deposition rate of 0.1 m/hr associated with strata produced by climbing bedforms (Allen, 1970, 1971; Rubin and Hunter, 1982)). Using the measured thicknesses of the same strata, we estimated a median minimum duration of deposition to be 2 hours. We refer to these values as minimum durations because climbing bedform deposits sometimes transition vertically to plane-laminated deposits within the same bed. It is not currently possible to estimate the duration of deposition associated with plane-laminated deposits. These durations are also a conservative estimate of flood durations, as we can expect the preserved depositional record to primarily represent sedimentation that occurred during waning flow after the flood peak. Furthermore, these estimates are spatially averaged; they encompass deposits at different elevations along the channel bank and on the proximal floodplain, and therefore inherently integrate variability in durations for which they were inundated.

Tabular floodplain sandstones are regularly interspersed within thinly laminated claystone and siltstone through the stratigraphy adjacent to and above the upper channel body. Floodplain sandstones are interpreted as crevasse deposits that are products of floods capable of suspending <200 µm sand. Supported by the description of Terry et al. (2001), who characterized floodplain paleosols in this section as weakly developed inceptisols, we infer that Orella floodplains were dynamic, and frequently inundated by floods associated with significant discharge variability in the adjacent ephemeral streams. We speculate that heightened seasonality, thought to be associated with the onset of the EOT (Wade et al., 2012), may be reflected in significant variability in river discharge, frequent overbank deposition and the ephemeral nature of the river channels.

Above the upper sand body and below the Serendipity Ash, we recorded several erosional surfaces that are interpreted to have formed through channel incision (Fig. S2). In general, erosional surfaces are overlain by flat lying mudstones or thinly bedded sandstones that onlap the margins of the erosional surface. One of the erosional features is draped by volcanic ash that preserves ~3.6 m of erosional relief. Another erosional surface is overlain by ~2m of inclined, fining-upward, medium-bedded sandstones interpreted as weathered channel bar deposits.

We assumed two major erosional episodes punctuated by less significant filling and incision events. The first and second episode produced maximum erosional relief of approximately 10.8 m and 4 m respectively. Elsewhere in TGP, (Sahy et al., 2015) measured two separate ash draped erosional scours with approximate erosional relief of 15 m and 5 m, draped by the Horus and Serendipity ashes respectively. From the dominance of fine-grained fill in the erosional scours, we infer that, with the exception of the single set of inclined beds, the mapped exposures primarily intersect the channel scours away from the axes of the channels. We interpret the observed fill to primarily be floodplain and crevasse splay deposits, and infer that the true magnitude of erosional relief may be underestimated.

3.2. Recurrent episodes of erosion and fill

Our peak discharge estimates from flood-deposited sandstones are unremarkable; however, the recurrent episodes of sustained channel incision and fill suggest transience on early Oligocene fluvial landscapes that may have been caused by variability in external influences that altered discharge or ratios of water to sediment flux through the formative channels. We speculate that recurrent erosion may have been the result of one or both of two possible factors. First, during the ~300,000 year period at the onset of the EOT, atmospheric carbon dioxide (CO_2) concentrations fluctuated between ~1,100 p.p.m.v. to <750 p.p.m.v.(Zachos et al., 2001). We speculate that the incumbent variability in atmospheric and oceanic circulation patterns (Zachos et al., 2001), may have produced significant instability in the terrestrial climate and, by extension, river landscapes of North America. Second, volcanogenic sediment from Great Basin volcanism, delivered by eolian or river transport may have been responsible for sporadic increases in sediment fluxes through the rivers studied here. A temporary pulse of increased sediment flux would cause steepening and aggradation of the beds of rivers; once sediment fluxes returned to their original state, river slopes would decrease and channels would incise. Thus, the patterns of recurrent erosion and fill recorded in the OM fluvial strata could be the result of unsteadiness in climate and/or volcanogenic sediment supply. However, the data collected for this study is insufficient to fully explore either hypothesis.

3.3. Hydrology of Rivers and Catchments in Nebraska: Oligocene versus Modern

Mean annual precipitation (MAP) in the catchments of most of the modern streams included in this study (excepting the Ninnescah) range from ~400mm to ~600 mm (Fig. 4C). These values are less than the ~739 mm estimated MAP for the early Oligocene at TGP (Terry et al., 2001). Our reconstructed river discharges (~168 cms) from early Oligocene TGP strata are an order of magnitude greater than most of the modern streams surveyed in our data-set (Fig. 4D). Together, these data suggest that moisture availability was greater on early Oligocene river landscapes preserved at TGP than it is today.

Interestingly, sediment transport reconstruction through early Oligocene rivers scale well with the modern North Loup (Mohrig, 1994) and Calamus (Gabel, 1993) rivers. Longitudinal river slopes in sand-bedded rivers are controlled by the ratio of sediment flux to water flux. We therefore conclude that the order of magnitude differences in longitudinal gradient and discharge resulted in similar estimates of sediment flux for modern and ancient streams.

3.4. Dynamic Topography and Post-depositional Tilting of early Oligocene Strata at Toadstool Geologic Park

Crustal shortening and tectonic uplift associated with the Laramide orogeny ceased by the late Eocene (Sjostrom et al., 2006; Mix et al., 2011; Chamberlain et al., 2012; Fan et al., 2014a, 2014b); however, post-orogenic differential uplift, generally thought to have initiated during the Miocene ~6Ma and believed to be continuing today, appears to be driving a west-to-east tilting of the Great Plains (Heller et al., 2003; Fernandes and Roberts, 2021) (McMillan et al., 2002, 2006; Leonard, 2002; Heller et al., 2003; Duller et al., 2012; Marder et al., 2024) (Moucha et al., 2008, 2009; Karlstrom et al., 2012; Hansen et al., 2013; Rosenberg et al., 2014) ; (Abbey et al., 2018; Abbey and Niemi, 2018) (Fernandes and Roberts, 2021); (Mitrovica et al., 1989; Tucker and van der Beek, 2013).

Our early Oligocene estimates of river long profiles provide an estimate of post-Laramide river slopes, before significant tilting associated with dynamic topography occurred. The eastward flowing sand-bedded rivers that created the TGP strata possessed longitudinal slopes of ~10^{-4}; the west-to-east average slope of the landscape surface today is ~ 10^{-3} (measured with Google Earth) and the longitudinal slopes of modern rivers is also ~ 10^{-3} (Fig. 4B). These estimates support an inference that post-Laramide dynamic topography altered river longitudinal slopes by approximately one order of magnitude.

McMillan et al., 2002, estimated that the Miocene-Pliocene fluvial strata (17.5 - 5 Ma) of the Ogallala Group, exposed in the Cheyenne Tablelands Wyoming and Nebraska and now tilting down towards the east at slopes as great as 10^{-2}, represent longitudinal fluvial slopes of 10^{-4} - 10^{-3}. From these combined estimates, we infer that river longitudinal slopes remained relatively stable from ~33.9 Ma - 17.5 Ma; however, further data from strata associated with the intervening period is necessary to confirm this.

3.5. Dynamic Floodplains and Catchment-scale of Environmental Information

Cuticular wax δD values range from -150.79‰ to -170.34‰ from channel strata and -151.99‰ to -164.37‰ in floodplain strata, with the median δD from each depositional facies being -160.71‰ and -159.66‰, respectively. Organic carbon δ^{13}C values were also quite similar, ranging from -26.6‰ to -30.1‰ from channel deposits and -27.7‰ to -29‰ in floodplain deposits, with the medians being -27.7‰ and -28.4‰ for channel and floodplain strata respectively. ACL values range from -29.04 to -29.56 in channel strata and -27.7 to –28.4 in floodplain strata, with median values of 29.24 and 29.34 respectively. Thus, environmental information recovered from channels and floodplains was more similar than different.

From the similar paleoenvironmental signals in channels and floodplains, we infer that Orella Member channel and floodplain strata primarily recorded catchment-integrated information inherited from transported sediment. Our inference is supported by our characterization of OM floodplains as dynamic, and the pedological classification of floodplain paleosols as inceptisols (Terry et al., 2001). Inceptisols can be expected to form on floodplains that were frequently inundated and not static long enough to develop mature soils or build up sufficient biomass to overprint the catchment-averaged environmental information with *in situ* information from local plant communities.

3.6. Paleo-relief and Paleo-elevations of Fossilized Rivers and Catchments, during the Oligocene

The mean δD lapse rate of modern river water (7.6 ‰ per degree longitude) is similar to Eocene through modern estimates (Fan et al., 2014a). On this basis, we assumed that altitude-driven δD lapse rates during the Oligocene were similar to modern lapse rates. We estimated a δD lapse rate of -23.6 ‰ per km elevation increase for modern drainage basins in the Great Plains (Kendall and Coplen, 2001). We inferred that the most depleted δD values recovered from ancient cuticular waxes represent transported plant carbon derived from high elevations in the paleo-catchment and the most enriched values represent plant communities living at the paleo-elevation of the local rivers and floodplains. Thus, the difference between maximum and minimum δD values can be used to estimate the relief of the catchment relative to the elevation of the studied river deposits during the early Oligocene. With these initial assumptions, we estimated a mean catchment relief of ~870 m (0.86 km).

We explored potential pathways for constraining the paleo-elevation of early Oligocene rivers of TGP and the catchments that fed them. The work of (Müller et al., 2018) indicates that the TGP region has uplifted a total of 500m since the Oligocene. TGP lies at approximately 1100 m above sea-level today Fig. 1). Reconstructed sea-level estimates suggest that during the early Oligocene period in question (33.9 - 33.4 Ma), global sea-level was ~25m lower than today (Miller et al., 2020). With the help of these estimates we infer that the rivers and floodplain sediments studied here were deposited at approximately 625 m above sea-level. Combined with our estimates of paleo-relief, high elevations within the feeder catchments were approximately 1.6 km.

5 Summary

The early Oligocene was a pivotal period in earth's history; it marks the beginning of the Eocene

Oligocene Transition when global climate had begun the long term transition from a greenhouse state to a to a cooler and drier icehouse state (Fischer, 1982), when global sea surface temperatures cooled by ~6 ºC (Coxall et al., 2005) and when the first permanent ice sheets of the Cenozoic developed on Antarctica (Ivany et al., 2003, 2006; Galeotti et al., 2016). Fluctuating atmospheric CO_2 concentrations introduced significant variability in oceanic and atmospheric circulation over a period of ~300,000 years (Zachos et al., 2001).

Early Oligocene landscapes in North America, thought to be tectonically quiet after the final stages of Laramide uplift ended a ~40 Ma, may have been influenced by enhanced seasonality and increasingly cold winters in the Gulf of Mexico (Wade et al., 2012) and fluctuations in volcanogenic sediment supplied by the Great Basin volcanism. While a substantial body of work has helped to resolve patterns of climate change, tectonic activity and volcanism in the continental interior of North America during this period of time, the characteristics of rivers, floodplains and catchments during this period are relatively understudied.

We employed a coordinated approach to couple descriptive and quantitative reconstructions of (a) flow, sediment transport, migration and avulsion patterns through river channels, (b) the dynamics of their adjacent floodplains, and (c) catchment-scale reconstructions of variability in moisture availability and ecosystem function, from early Oligocene fluvial strata (~33.9 Ma - ~ 33.4 Ma) of the Orella Member of the Brule Formation of the White River Group, exposed at Toadstool Geologic Park, Nebraska, U. S. A.

We briefly summarize our key conclusions below:

(1) From two preserved channel sand bodies, we estimated that the studied rivers had flow depths that were approximately 2.5 and widths that were 65 m wide. The lower channel sand body is anomalously thick (5-6 m; 2-3 times peak flow depth), from which we inferred that formative channels were confined within an erosional corridor with 5m - 11m of relief. The upper channel sand body

thickness is less than 1.5 times estimated peak flow depth, suggesting that it was free to avulse without erosional confinement.

(2) Rivers were ephemeral; estimated median peak discharges were ~ 168 m^3/s, and subaerial exposure surfaces on the beds of river channels suggest that base flow was equal to or close to zero.

(3) Measured modern annual precipitation is 100-200 mm less than reconstructions (Terry et al., 2001) of ~739 mm. Reconstructed discharges are an order of magnitude larger than discharge through most modern rivers in the region. Together, these estimates suggest that modern landscapes in the region have significantly less available moisture.

(4) Floodplains were dynamic; overbank floods were capable of suspending up to 200 μm sand which was deposited in extensive and recurrent sheets interspersed with floodplain mudstones. Floodplain soils were described by Terry et al. (2001) as primarily inceptisols, which are characteristic of relatively dynamic landscapes with floodplains that are not stable long enough to generate mature soils and/or cooler drier climes.

(5) Floodplain and channel strata record similar paleoenvironmental signals (δD, $\boldsymbol{\delta^{13}C}$, ACL), from which we inferred that the recovered information was primarily catchment-integrated and inherited from transported sediment.

(6) Reconstructed paleo-catchment relief, estimated from variability in δD values and modern altitude drive lapse rates, was ~800m.

(7) Estimated paleoelevation of early Oligocene river landscapes preserved and exposed at Toadstool Geologic Park, based on published estimates of local uplift and sea-level, of early Oligocene rivers preserved was ~625m above sea-level.

(8) Channels had a gradient of approximately 3×10^{-4} , which is an order of magnitude less than modern rivers in the region. We inferred that eastward tilting of the Great Plains of Nebraska, associated with dynamic topography thought to have initiated during the Miocene produced a change in river longitudinal slopes from the early Oligocene to the present.

(9) Median unit bedload flux of 4×10^{-5} m^2/s is similar to the modern North Loup River. Reconstructed dune heights were approximately 0.3 m, which is similar in scale to measurements from the North Loup and Calamus Rivers. We attribute the similarity in modern and ancient sediment fluxes to the larger modern river gradients coupled with smaller modern water discharges.

(10) While our peak discharge estimates from flood-deposited sandstones are unremarkable, we found compelling evidence for recurrent episodes of channel incision and fill. Reconstructed erosional relief is significantly greater than our estimates of flow depth. Our largest estimate of erosional relief was ~11m while other workers have estimated erosional relief as great as 15m ((Sahy et al., 2015)). We theorize that repeated episodes of erosion and fill may have been the result of unsteadiness in climate and/or volcanogenic sediment supply, but further work is needed to explore these hypotheses.

Our work advances the state of knowledge under two key themes:

First, we deliver a detail-rich characterization of early Oligocene North American landscapes in the Toadstool Geological Park region of Nebraska during this pivotal period in earth history when North American landscapes had transitioned from humid forests of the Eocene to open, treeless, semi-arid, seasonally wet savannas seen today (Terry et al., 2001). Our results offer insight into river and catchment hydrology and hydrological variability, landscape morphology and dynamics, paleo-elevation and paleo-relief, post-depositional tilting and the differences between early Oligocene and modern landscapes on the High Plains of northwestern Nebraska.

Second, we develop a coordinated workflow to check for internal consistency between reconstructions of catchment-scale hydroclimatic variability from paleoenvironmental proxies, the dynamics of rivers and floodplains, and the fluxes of sediment and water routed through or stored by the transport system. Such paired climate-and-river reconstructions are particularly powerful because they deliver estimates of climate, flow and sediment transport on temporal and spatial scales that are compatible with predictive hydraulic and sediment transport modeling tools and they bridge the timescale gap between hindcasts from the geologic record, modern hydrological data with hourly to decadal resolution, and model forecasts generated on hourly to millennial time-scales.

6. Acknowledgements

Funding for this research was provided by the National Science Foundation (Grant EAR-2023710), Denison University Research Fund, Denison University's Provost's Office and Denison's Anderson Summer Scholars program. We thank Christopher Sparacio (Univ. Connecticut) for field assistance and Denison University undergraduate field and lab assistants Linda Contreras Garcia, TJ Cracas, George Fox, Anna Grendys, Tricia Klosterman, Laura Lapham, Thea Pederson, Andi Scroggs, and Nay Woodley.

7. Manuscript Figures

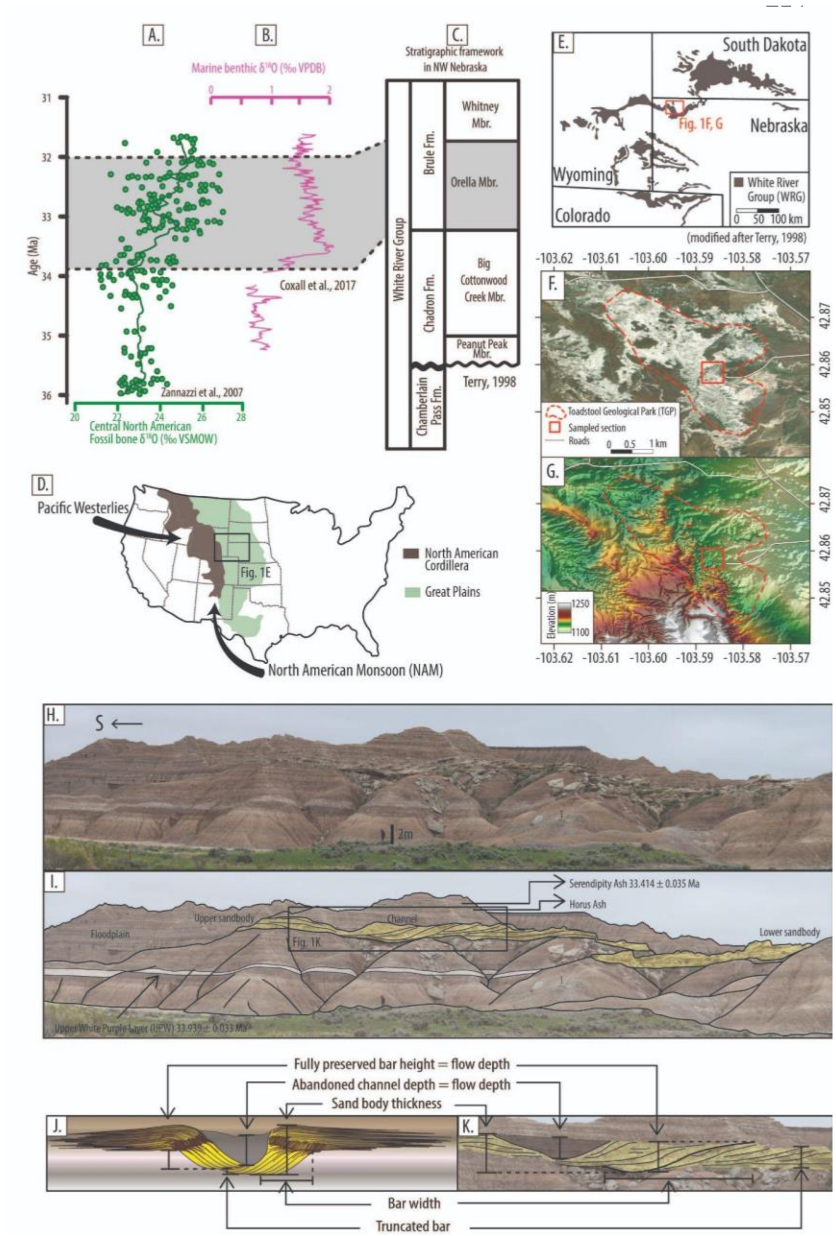

Figure 1: A) Terrestrial record of oxygen isotopic ratios from mammal tooth enamel and bone, in the White River Group, data from Zanazzi et al., 2007, replotted here. B) Marine record of oxygen isotopic variation from marine benthic organisms, data from Coxall et al., 2005. C) The stratigraphic units at Toadstool Geologic Park. D) Regional context for the study. E) Outcrops of the White River Group, with regional location indicated by the black rectangle in 1D. F) Satellite image, and G) Elevation map draped with a hillshade map showing the study location. H) Photograph, with I) annotated overlay, showing locations of dated ash beds and the lower and upper channel bodies. J) simplified cartoon, and K) annotated outcrop (location shown by black rectangle in I) indicating key measurements collected at channel outcrops.

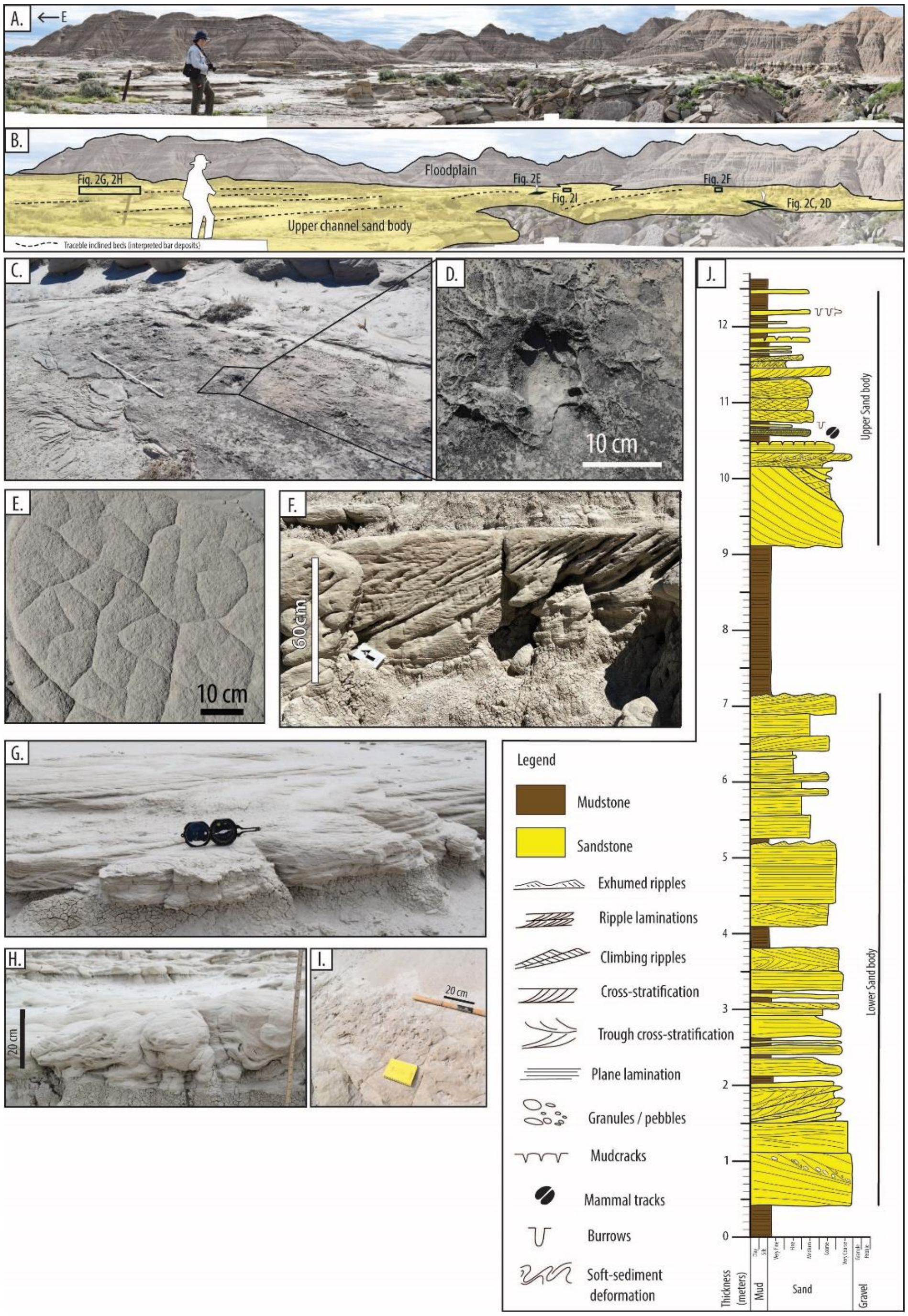

Figure 2:

A) Perspective image of the upper channel body, with B) annotations indicating the locations of key sedimentary structures, including C) mammal tracks superimposed on a ripple reworked compound bedform, D) sediment splatter around a hoof print, E) mud cracks on the channel bed, F) inclined bar strata with internal stratification from climbing dunes and super-critically climbing ripples, G) ripple laminations in bar strata, H) soft sediment deposition in bar strata, and I) burrows on the channel bed. J) A composite stratigraphic column through the lower and upper sand bodies.

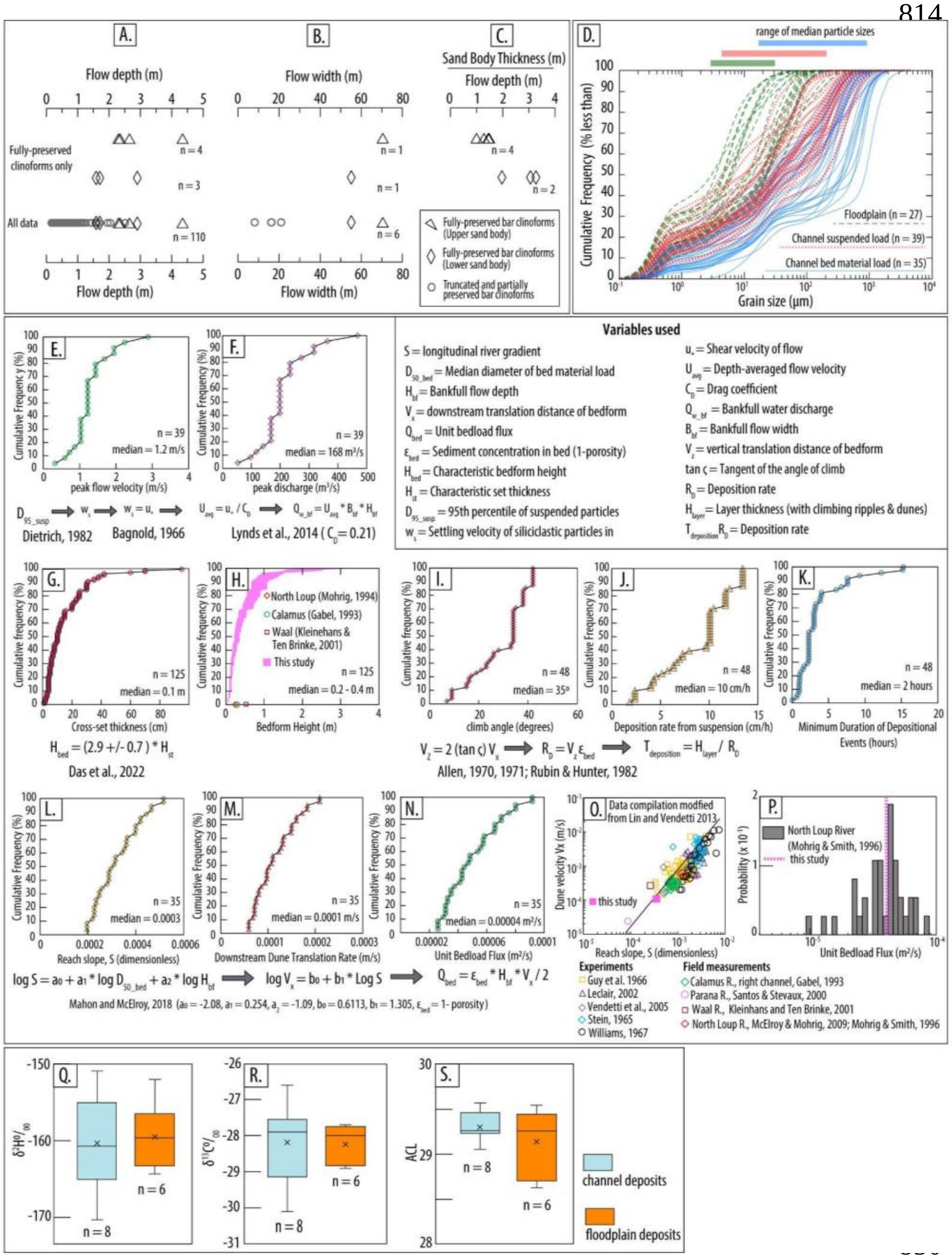

Figure 3: A) Flow depth estimates from bar clinoform thicknesses. B) Flow width estimates from cross-stream widths of bar clinoforms. C) Ratios of sand body thickness to flow depth. D) Grain size distributions of all sediment samples. Cumulative frequency distributions of E) estimated depth-averaged velocity at peak discharge, F) estimated peak discharge, G) measured cross set thickness, H) estimated bedform heights, I) measured angle of climb in climbing bedform strata, J) estimated deposition rate from suspension, K) estimated minimum duration of depositional events, L) estimated reach slope, .) estimated downstream dune translation rate, and N) estimated unit bedload flux. O) Estimates of dune slope and dune velocity compared against a compilation of experimental and modern river measurements from Lin & Vendetti (2013) on which the method is based. P) Estimated median unit bedload flux compared against estimates from the North Loup River. Measurements of Q) δD, R) δ^{13}C, and S) Average chain length of *n*-alkanes.

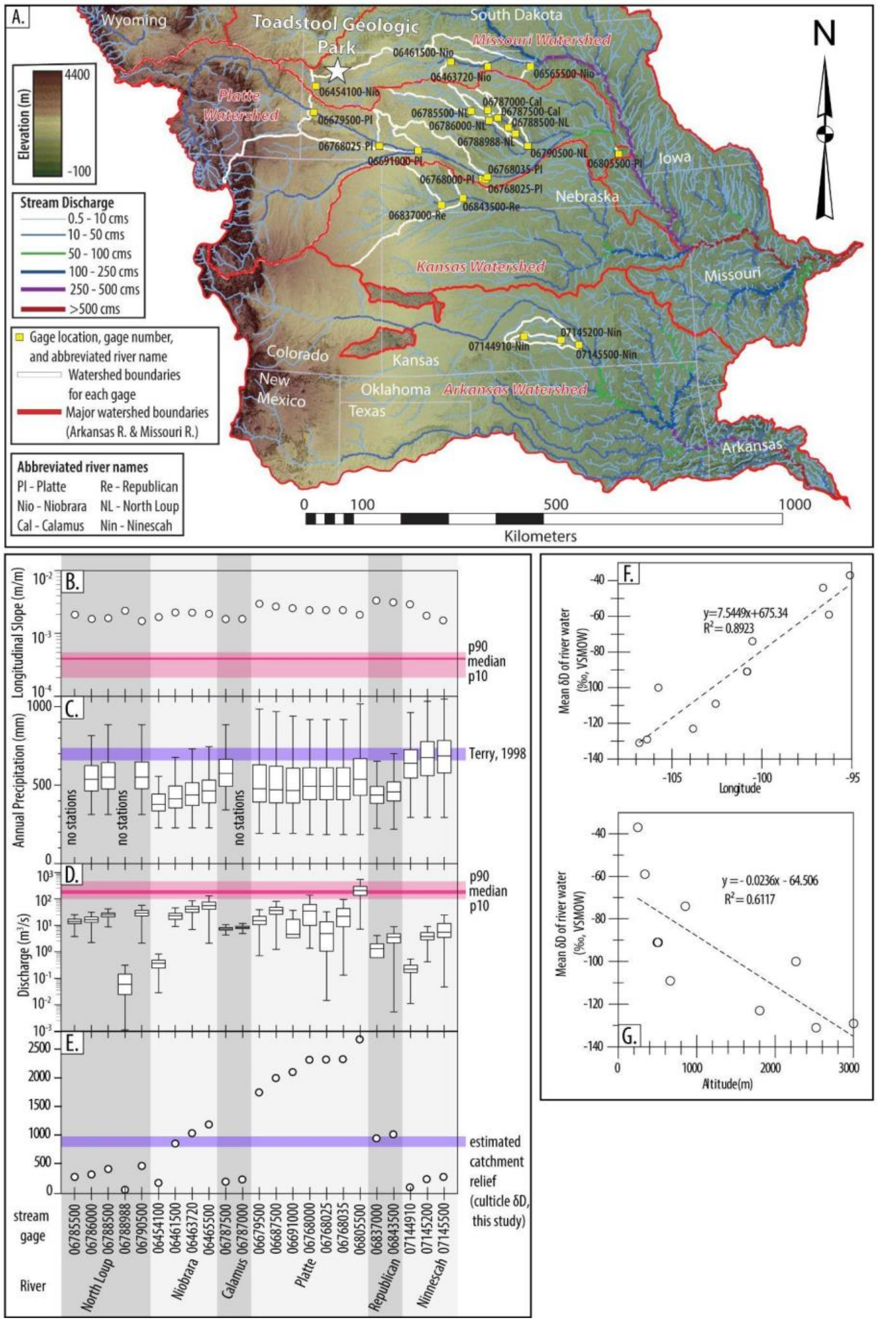

Figure 4: A) Locations of 23 stream gauges and their catchments. Data collected for each stream gauge includes B) Longitudinal slope of stream, C) distributions of annual precipitation, D) distributions of discharges, and E) catchment relief. Shaded horizontal bars show reconstructed values in B- E. Whiskers indicate 10th and 90th percentile, boxes indicate 25th and 75th percentiles, bars indicate median in C and D. Change in δD values with F) longitude, and G) Altitude.

8. References cited

Abbey, A.L., and Niemi, N.A., 2018, Low-temperature thermochronometric constraints on fault initiation and growth in the northern Rio Grande rift, upper Arkansas River valley, Colorado, USA: Geology, v. 46, p. 627–630.

Abbey, A.L., Niemi, N.A., Geissman, J.W., Winkelstern, I.Z., and Heizler, M., 2018, Early Cenozoic exhumation and paleotopography in the Arkansas River valley, southern Rocky Mountains, Colorado: Lithosphere, v. 10, p. 239–266.

Allen, J.R.L., 1970, A quantitative model of climbing ripples and their cross-laminated deposits: Sedimentology, v. 14, p. 5–26.

Allen, J.R.L., 1971, Instantaneous sediment deposition rates deduced from climbing-ripple cross-lamination: Journal of the Geological Society, v. 127, p. 553–561.

Bagnold, R.A., 1966, An Approach to the Sediment Transport Problem from General Physics: U.S. Government Printing Office, 37 p.

Best, M.G., Barr, D.L., Christiansen, E.H., Gromme, S., Deino, A.L., and Tingey, D.G., 2009, The Great Basin Altiplano during the middle Cenozoic ignimbrite flareup: insights from volcanic rocks: International geology review, v. 51, p. 589–633.

Best, M.G., Christiansen, E.H., and Gromme, S., 2013, Introduction: The 36–18 Ma southern Great Basin, USA, ignimbrite province and flareup: Swarms of subduction-related supervolcanoes: Geosphere, v. 9, p. 260–274.

Blum, M.D., Milliken, K.T., Pecha, M.A., Snedden, J.W., Frederick, B.C., and Galloway, W.E., 2017, Detrital-zircon records of Cenomanian, Paleocene, and Oligocene Gulf of Mexico drainage integration and sediment routing: Implications for scales of basin-floor fans: Geosphere, v. 13, p. 2169–2205.

Boardman, G.S., and Secord, R., 2013, Stable isotope paleoecology of White River ungulates during the Eocene–Oligocene climate transition in northwestern Nebraska: Palaeogeography, palaeoclimatology, palaeoecology, v. 375, p. 38–49.

Bobik, T., 2021, A multiproxy approach to interpreting aridity across the Eocene-Oligocene Transition of the northern Great Plains (White River group), North America: Temple University, doi:10.34944/DSPACE/7221.

Bush, R.T., and McInerney, F.A., 2013, Leaf wax n-alkane distributions in and across modern plants: Implications for paleoecology and chemotaxonomy: Geochimica et cosmochimica acta, v. 117, p. 161–179.

Cardenas, B.T., Mohrig, D., and Goudge, T.A., 2020, The anatomy of exhumed river-channel belts: Bedform to belt-scale river kinematics of the Ruby Ranch Member, Cretaceous Cedar Mountain Formation, Utah, USA:, https://onlinelibrary.wiley.com/doi/abs/10.1111/sed.12765?casa_token=VwesNebR1CMAAAAA:niCLrN5ZoyGw4rx-xZpfgo_t5gxFVLOIRFjIG0F0KITiAPMJESQsyYKfAJSa_BZIumBlEwyuah4BYV8.

Cather, S.M., Chapin, C.E., and Kelley, S.A., 2012, Diachronous episodes of Cenozoic erosion in southwestern North America and their relationship to surface uplift, paleoclimate, paleodrainage, and paleoaltimetry: Geosphere, v. 8, p. 1177–1206.

Chamberlain, Mix, Mulch, and Hren, 2012, The Cenozoic climatic and topographic evolution of the western North American Cordillera: American journal of physiology. Renal physiology, https://www.ajsonline.org/content/312/2/213.short.

Chamberlin, E.P., and Hajek, E.A., 2019, Using bar preservation to constrain reworking in channel-dominated fluvial stratigraphy: Geology, v. 47, p. 531–534.

Chang, Q., Hren, M.T., Lai, L.S.-H., Dorsey, R.J., and Byrne, T.B., 2023, Rapid topographic growth of the Taiwan orogen since ~1.3-1.5 Ma: Science advances, v. 9, p. eade6415.

Coxall, H.K., Wilson, P.A., Pälike, H., Lear, C.H., and Backman, J., 2005, Rapid stepwise onset of Antarctic glaciation and deeper calcite compensation in the Pacific Ocean: Nature, v. 433, p. 53–57.

Das, D., Ganti, V., Bradley, R., Venditti, J., Reesink, A., and Parsons, D.R., 2022, The influence of transport stage on preserved fluvial cross strata: Geophysical research letters, v. 49, doi:10.1029/2022gl099808.

DeCelles, P.G., 2004, Late Jurassic to Eocene evolution of the Cordilleran thrust belt and foreland basin system, western U.S.A: American journal of science, v. 304, p. 105–168.

Diefendorf, A.F., Mueller, K.E., Wing, S.L., Koch, P.L., and Freeman, K.H., 2010, Global patterns in leaf 13C discrimination and implications for studies of past and future climate: Proceedings of the National Academy of Sciences of the United States of America, v. 107, p. 5738–5743.

Dietrich, W.E., 1982, Settling velocity of natural particles: Water Resources Research, v. 18, p. 1615–1626.

Duller, R.A., Whittaker, A.C., Swinehart, J.B., Armitage, J.J., Sinclair, H.D., Bair, A., and Allen, P.A., 2012, Abrupt landscape change post–6 Ma on the central Great Plains, USA: Geology, v. 40, p. 871–874.

Eley, Y.L., and Hren, M.T., 2018, Reconstructing vapor pressure deficit from leaf wax lipid molecular distributions: Scientific reports, v. 8, p. 3967.

Fan, M., Ayyash, S.A., Tripati, A., Passey, B.H., and Griffith, E.M., 2018, Terrestrial cooling and changes in hydroclimate in the continental interior of the United States across the Eocene-Oligocene boundary: GSA Bulletin, v. 130, p. 1073–1084.

Fan, M., and Dettman, D.L., 2009, Late Paleocene high Laramide ranges in northeast Wyoming: Oxygen isotope study of ancient river water: Earth and planetary science letters, v. 286, p. 110–121.

Fan, M., Feng, R., Geissman, J.W., and Poulsen, C.J., 2020, Late Paleogene emergence of a North American loess plateau: Geology, v. 48, p. 273–277.

Fan, M., Heller, P., Allen, S.D., and Hough, B.G., 2014a, Middle Cenozoic uplift and concomitant drying in the central Rocky Mountains and adjacent Great Plains: Geology, v. 42, p. 547–550.

Fan, M., Hough, B.G., and Passey, B.H., 2014b, Middle to late Cenozoic cooling and high topography in the central Rocky Mountains: Constraints from clumped isotope geochemistry: Earth and planetary science letters, v. 408, p. 35–47.

Farquhar, G.D., Ehleringer, J.R., and Hubick, K.T., 1989, Carbon Isotope Discrimination and Photosynthesis: Annual review of plant biology, v. 40, p. 503–537.

Fernandes, A.M., Hren, M., Smith, V.B., Singh, A., Terry, D.O., and Florida, O. River floodplains, organic carbon, and paleoclimate: How river dynamics impart biases in the biogeochemical climate record of terrestrial landscapes:, https://eartharxiv.org/repository/view/6624/.

Fernandes, V.M., and Roberts, G.G., 2021, Cretaceous to Recent net continental uplift from paleobiological data: Insights into sub-plate support: GSA Bulletin, v. 133, p. 1217–1236.

Fischer, A.G., 1982, Long-term climate oscillations recorded in stratigraphy: Climate in Earth history., p. 97–104.

Gabel, S.L., 1993, Geometry and kinematics of dunes during steady and unsteady flows in the Calamus River, Nebraska, USA: Sedimentology, v. 40, p. 237–269.

Galeotti, S. et al., 2016, Antarctic Ice Sheet variability across the Eocene-Oligocene boundary climate transition: Science, v. 352, p. 76–80.

Galloway, W.E., Whiteaker, T.L., and Ganey-Curry, P., 2011, History of Cenozoic North American drainage basin evolution, sediment yield, and accumulation in the Gulf of Mexico basin: Geosphere, v. 7, p. 938–973.

Gat, J.R., 1996, Oxygen and hydrogen isotopes in the hydrologic cycle: Annual review of earth and planetary sciences, https://www.annualreviews.org/doi/abs/10.1146/annurev.earth.24.1.225.

Grandstaff, D.E., and Terry, D.O., Jr, 2009, Rare earth element composition of Paleogene vertebrate fossils from Toadstool Geologic Park, Nebraska, USA: Applied geochemistry: journal of the International Association of Geochemistry and Cosmochemistry, https://www.sciencedirect.com/science/article/pii/S0883292708004617.

Greenberg, E., Ganti, V., and Hajek, E., 2021, Quantifying bank full flow width using preserved bar clinoforms from fluvial strata: Geology, v. 49, p. 1038–1043.

Hansen, S.M., Dueker, K.G., Stachnik, J.C., Aster, R.C., and Karlstrom, K.E., 2013, A rootless rockies-Support and lithospheric structure of the Colorado Rocky Mountains inferred from CREST and TA seismic data: Geochemistry, Geophysics, Geosystems, v. 14, p. 2670–2695.

Heller, P.L., Dueker, K., and McMillan, M.E., 2003, Post-Paleozoic alluvial gravel transport as evidence of continental tilting in the U.S. Cordillera: GSA Bulletin, v. 115, p. 1122–1132.

Holloway, P.J., 1969, The effects of superficial wax on leaf wettability: The Annals of applied biology, v. 63, p. 145–153.

Humphreys, E.D., 1995, Post-Laramide removal of the Farallon slab, western United States: Geology, v. 23, p. 987–990.

Ivany, L.C., Van Simaeys, S., Domack, E.W., and Samson, S.D., 2006, Evidence for an earliest Oligocene ice sheet on the Antarctic Peninsula: Geology, v. 34, p. 377–380.

Ivany, L.C., Wilkinson, B.H., and Jones, D.S., 2003, Using Stable Isotopic Data to Resolve Rate and Duration of Growth throughout Ontogeny: An Example from the Surf Clam, Spisula solidissima: Palaios, v. 18, p. 126–137.

Karlstrom, K.E. et al., 2012, Mantle-driven dynamic uplift of the Rocky Mountains and Colorado Plateau and its surface response: Toward a unified hypothesis: Lithosphere, v. 4, p. 3–22.

Kendall, C., and Coplen, T.B., 2001, Distribution of oxygen-18 and deuterium in river waters across the United States: Hydrological processes, v. 15, p. 1363–1393.

Kleinhans Maarten G., and Brinke Wilfried B. M. Ten, 2001, Accuracy of Cross-Channel Sampled Sediment Transport in Large Sand-Gravel-Bed Rivers: Journal of Hydraulic Engineering, v. 127, p. 258–269.

Korus, J.T., and Joeckel, R.M. Exhumed fluvial landforms reveal evolution of late Eocene–Pliocene rivers on the Central and Northern Great Plains, USA: Geosphere, doi:10.1130/GES02587.1.

LaGarry, H.E., 1998, Lithostratigraphic revision and redescription of the Brule Formation (White River Group) of northwestern Nebraska, *in* Terry, D.O., LaGarry, H.E., and Hunt, R.M. eds., Depositional Environments, Lithostratigraphy, and Biostratigraphy of the White River and Arikaree Groups (Late Eocene to Early Miocene, North America), p. 63–92.

Larson, E.E., and Evanoff, E., 1998, Tephrostratigraphy and source of the tuffs of the White River sequence, *in* Terry, D.O., LaGarry, H.E., and Hunt, R.M. eds., Depositional Environments, Lithostratigraphy, and Biostratigraphy of the White River and Arikaree Groups (Late Eocene to Early Miocene, North America), researchgate.net, p. 1–14.

Lauretano, V., Kennedy-Asser, A.T., Korasidis, V.A., Wallace, M.W., Valdes, P.J., Lunt, D.J., Pancost, R.D., and Naafs, B.D.A., 2021, Eocene to Oligocene terrestrial Southern Hemisphere cooling caused by declining pCO2: Nature geoscience, v. 14, p. 659–664.

Leonard, E.M., 2002, Geomorphic and tectonic forcing of late Cenozoic warping of the Colorado piedmont: Geology, v. 30, p. 595–598.

Lipman, P.W., and McIntosh, W.C., 2008, Eruptive and noneruptive calderas, northeastern San Juan Mountains, Colorado: Where did the ignimbrites come from? GSA Bulletin, v. 120, p. 771–795.

Lukens, W., 2013, Paleopedology And Paleogeomorphology Of The Early Oligocene Orella And Whitney Members, Brule Formation, White River Group, Toadstool Geologic Park, Nebraska. MS Thesis.

Lynds, R.M., Mohrig, D., Hajek, E.A., and Heller, P.L., 2014, Paleoslope Reconstruction In Sandy Suspended-Load-Dominant Rivers: Journal of Sedimentary Research, v. 84, p. 825–836.

Mahon, R.C., and McElroy, B., 2018, Indirect estimation of bedload flux from modern sand-bed rivers and ancient fluvial strata: Geology, https://pubs.geoscienceworld.org/gsa/geology/article-abstract/46/7/579/531398.

Marder, E., Gallen, S.F., and Pazzaglia, F.J., 2024, Late Cenozoic deformation in the U.S. southern Colorado Front Range revealed by river profile analysis and fluvial terraces: GSA Bulletin, v. 136, p. 1067–1085.

McElroy, B., and Mohrig, D. Nature of deformation of sandy bed forms: Journal of Geophysical Research, [Solid Earth], doi:10.1029/2008JF001220.

McMillan, M.E., Angevine, C.L., and Heller, P.L., 2002, Postdepositional tilt of the Miocene-Pliocene Ogallala Group on the western Great Plains: Evidence of late Cenozoic uplift of the Rocky Mountains: Geology, v. 30, p. 63–66.

McMillan, M.E., Heller, P.L., and Wing, S.L., 2006, History and causes of post-Laramide relief in the Rocky Mountain orogenic plateau: GSA Bulletin, v. 118, p. 393–405.

Miller, K.G., Browning, J.V., Schmelz, W.J., Kopp, R.E., Mountain, G.S., and Wright, J.D., 2020, Cenozoic sea-level and cryospheric evolution from deep-sea geochemical and continental margin records: Science Advances, v. 6, p. eaaz1346.

Miller, K.G., Fairbanks, R.G., and Mountain, G.S. Tertiary oxygen isotope synthesis, sea level history, and continental margin erosion: Paleoceanography, doi:10.1029/PA002i001p00001.

Mitrovica, J.X., Beaumont, C., and Jarvis, G.T., 1989, Tilting of continental interiors by the dynamical effects of subduction: Tectonics, v. 8, p. 1079–1094.

Mix, H.T., Mulch, A., Kent-Corson, M.L., and Page Chamberlain, C., 2011, Cenozoic migration of topography in the North American Cordillera: Geology, v. 39, p. 87–90.

Mohrig, D.C., 1994, Spatial evolution of dunes in a sandy river: University of Washington, 130 p., https://denison.idm.oclc.org/login?url=https://www.proquest.com/dissertations-theses/spatial-evolution-dunes-sandy-river/docview/304143877/se-2.

Mohrig, D., Heller, P.L., Paola, C., and Lyons, W.J., 2000, Interpreting avulsion process from ancient alluvial sequences: Guadalope-Matarranya system (northern Spain) and Wasatch Formation (western Colorado): GSA Bulletin, v. 112, p. 1787–1803.

Mohrig, D., and Smith, J.D. Predicting the migration rates of subaqueous dunes: Water resources research, doi:10.1029/96WR01129.

Moucha, R., Forte, A.M., Rowley, D.B., Mitrovica, J.X., Simmons, N.A., and Grand, S.P., 2009, Deep Mantle Forces and the Uplift of the Colorado Plateau: Geophysical research letters, doi:10.1029/2009GL039778.

Moucha, R., Forte, A.M., Rowley, D.B., Mitrovica, J.X., Simmons, N.A., and Grand, S.P., 2008, Mantle convection and the recent evolution of the Colorado Plateau and the Rio Grande Rift valley: Geology, v. 36, p. 439–442.

Müller, R.D., Cannon, J., Qin, X., and Watson, R.J., 2018, GPlates: Building a virtual Earth through deep time: Geochemistry: Exploration, Environment, Analysis, https://agupubs.onlinelibrary.wiley.com/doi/abs/10.1029/2018gc007584.

Neinhuis, C., and Barthlott, W., 1997, Characterization and Distribution of Water-repellent, Self-cleaning

Plant Surfaces: Annals of botany, v. 79, p. 667–677.

Poulsen, C.J., and Louise Jeffery, M., 2011, Climate change imprinting on stable isotopic compositions of high-elevation meteoric water cloaks past surface elevations of major orogens: Geology, v. 39, p. 595–598.

Prothero, D.R., and Emry, R.J., 1996, The Terrestrial Eocene-Oligocene Transition in North America: 704 p.

Retallack, G.J., 2007, Cenozoic Paleoclimate on Land in North America: The Journal of geology, v. 115, p. 271–294.

Retallack, G.J., 1992, Middle Miocene fossil plants from Fort Ternan (Kenya) and evolution of African grasslands: Paleobiology, v. 18, p. 383–400.

Rosenberg, R., Kirby, E., Aslan, A., Karlstrom, K., Heizler, M., and Ouimet, W., 2014, Late Miocene erosion and evolution of topography along the western slope of the Colorado Rockies: Geosphere, v. 10, p. 641–663.

Rubin, D.M., and Hunter, R.E., 1982, Bedform climbing in theory and nature: Sedimentology, v. 29, p. 121–138.

Sachse, D. et al., 2012, Molecular Paleohydrology: Interpreting the Hydrogen-Isotopic Composition of Lipid Biomarkers from Photosynthesizing Organisms: Annual review of earth and planetary sciences, v. 40, p. 221–249.

Sahy, D., Condon, D.J., Terry, D.O., Fischer, A.U., and Kuiper, K.F., 2015, Synchronizing terrestrial and marine records of environmental change across the Eocene–Oligocene transition: Earth and planetary science letters, v. 427, p. 171–182.

Santos, M.L., and Stevaux, J.C., 2000, Facies and architectural analysis of channel sandy macroforms in the upper Parana river: Quaternary international: the journal of the International Union for Quaternary Research, v. 72, p. 87–94.

Sato, Y., and Denson, N.M., 1967, Volcanism and tectonism as reflected by the distribution of nonopaque heavy minerals in some Tertiary rocks of Wyoming and adjacent states: U.S. Geological Survey Professional Paper, p. C42–C54.

Schimmelmann, A., Lange, C.B., Zhao, M., and Harvey, C., 1997, Southern California's megaflood event of ca. 1605 AD linked to large-scale atmospheric forcing:.

Schmandt, B., and Humphreys, E., 2010, Complex subduction and small-scale convection revealed by body-wave tomography of the western United States upper mantle: Earth and planetary science letters, v. 297, p. 435–445.

Schultz, B.C., and Stout, T.M., 1955, Classification of Oligocene Sediments in Nebraska: A Guide for the Stratigraphic Collecting of Fossil Mammals: Bulletin of the University of Nebraska State Museum, v. 4, p. 17–52.

Seminara, G., and Tubino, M., 1989, Alternate bars and meandering: Free, forced and mixed interactions, *in* River Meandering, Washington, D. C., American Geophysical Union, Water Resources

Monograph, p. 267–320.

Sheldon, N., 2009, Nonmarine records of climatic change across the Eocene-Oligocene transition: Geological Society of, v. 452, p. 241–248.

Sheldon, N.D., and Retallack, G.J., 2004, Regional Paleoprecipitation Records from the Late Eocene and Oligocene of North America: The Journal of geology, v. 112, p. 487–494.

Sjostrom, D.J., Hren, M.T., Horton, T.W., Waldbauer, J.R., and Page Chamberlain, C., 2006, Stable isotopic evidence for a pre–late Miocene elevation gradient in the Great Plains–Rocky Mountain region, USA: Geological Society of America, v. Special Paper 398, p. 309–319.

Terry, Jr, Dennis, O., 2001, Paleopedology of the Chadron Formation of Northwestern Nebraska: implications for paleoclimatic change in the North American midcontinent across the Eocene–Oligocene boundary: Palaeogeography, palaeoclimatology, palaeoecology, v. 168, p. 1–38.

Trampush, S.M., Huzurbazar, S., and McElroy, B., 2014, Empirical assessment of theory for bank full characteristics of alluvial channels: Water resources research, v. 50, p. 9211–9220.

Tucker, G.E., and van der Beek, P., 2013, A model for post-orogenic development of a mountain range and its foreland: Basin Research, v. 25, p. 241–259.

Wade, B.S., Houben, A.J.P., Quaijtaal, W., Schouten, S., Rosenthal, Y., Miller, K.G., Katz, M.E., Wright, J.D., and Brinkhuis, H., 2012, Multiproxy record of abrupt sea-surface cooling across the Eocene-Oligocene transition in the Gulf of Mexico: Geology, v. 40, p. 159–162.

Yang, H., Liu, W., Leng, Q., Hren, M.T., and Pagani, M., 2011, Variation in n-alkane δD values from terrestrial plants at high latitude: Implications for paleoclimate reconstruction: Organic geochemistry, v. 42, p. 283–288.

Zachos, J.C., Shackleton, N.J., Revenaugh, J.S., Pälike, H., and Flower, B.P., 2001, Climate response to orbital forcing across the Oligocene-Miocene boundary: Science, v. 292, p. 274–278.

Zanazzi, A., Kohn, M.J., MacFadden, B.J., and Terry, D.O., 2007, Large temperature drop across the Eocene–Oligocene transition in central North America: Nature, v. 445, p. 639–642.

9. Supplemental Information

Figure S-1: Map and perspective view of exhumed bar deposits and paleo-transport.

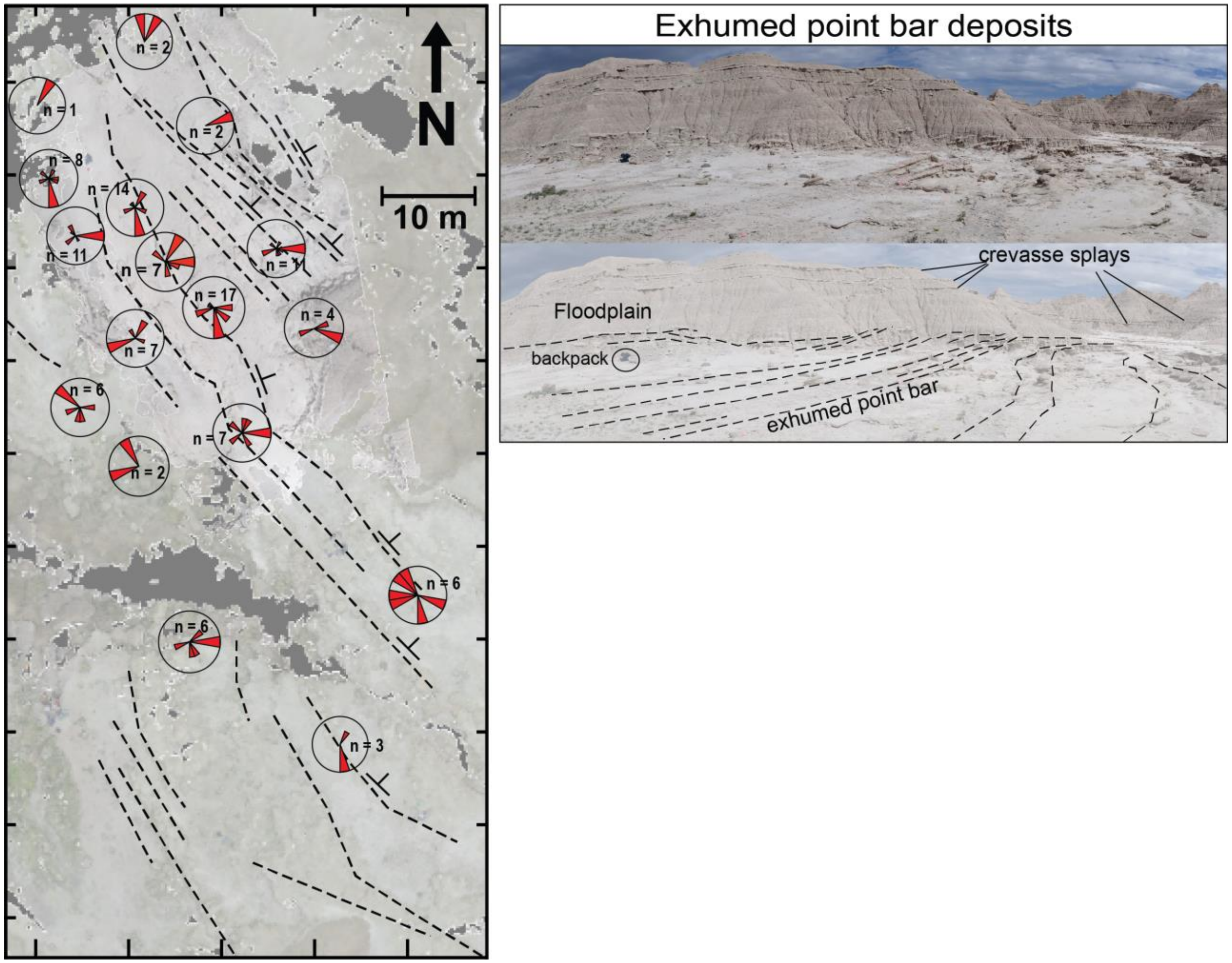

Figure S-2: Panoramic overview of recurrent erosional surfaces above the upper channel body

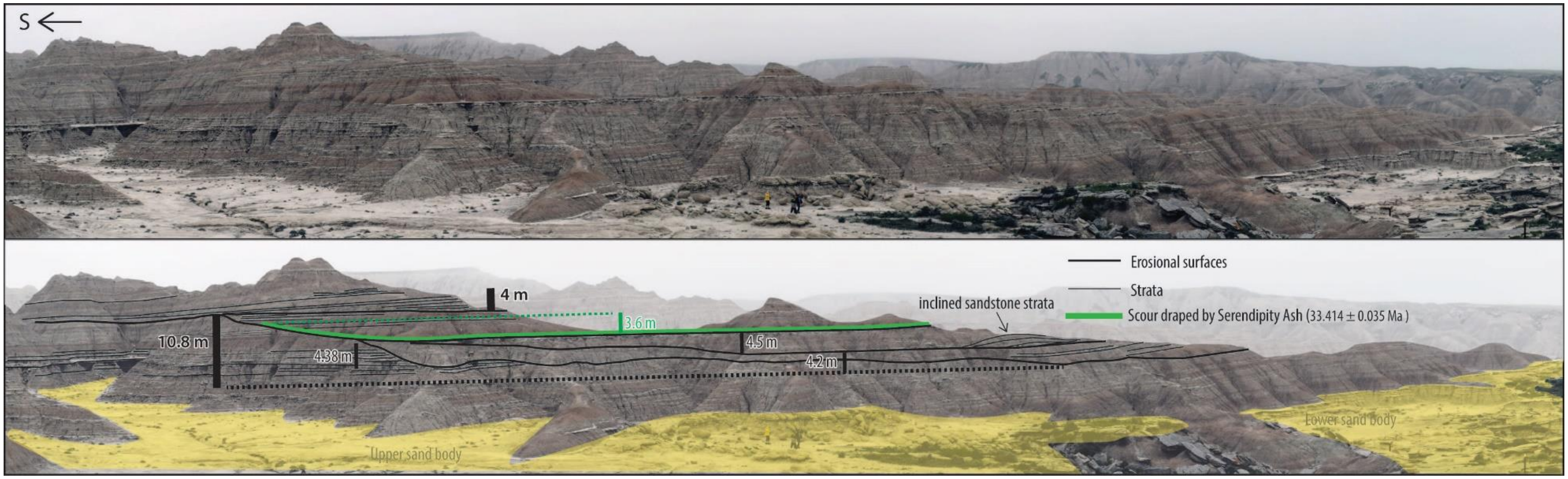

TABLE S-1.— LiDAR links to the Orella Member outcrops.

Area	Link to LiDAR
Orella Member - Lower sand body	http://potree.villanova.edu/ts2/ts2_1p7/
Orella Member - Upper sand body	http://potree.villanova.edu/toadstool1/

TABLE S-2.— Field measurement results of bar height, bar width, and sand body thickness of Orella Member (OM).

Bar Number	**Upper or Lower sand body**	**Bar Preservation**	**Type**	**Bar Height (m)**	**Sand Body Thickness (m)**	**Sand Body / Flow Depth**	**Bar Width (m)**	**Estimated Flow Width (m)**	**Supple. Fig. Index**
OM-Bar 66	Upper	Fully preserved	Bar clinoforms	4.35	4.35	1.00	30.31	70.93	Fig. S3(K)
OM-Bar 110	Upper	Fully preserved	Bar clinoforms	2.65	3.40	1.28	--	--	--
OM-Bar 111	Upper	Fully preserved	Bar clinoforms	2.35	3.40	1.45	--	--	--
OM-Bar 112	Upper	Fully preserved	Bar clinoforms	2.30	3.40	1.48	--	--	--
OM-Bar 49	Lower	Fully preserved	Bar clinoforms	1.59	6.50	4.09	23.83	55.76	Fig. S3(G)
OM-Bar 104	Lower	Fully preserved	Bar clinoforms	1.70	6.50	3.82	--	--	Fig. S3(R)
OM-Bar 110	Lower	Fully preserved	Bar clinoforms	2.82	5.26	1.87	--	--	Fig. S3(S)
OM-Bar 74	Upper	Truncated	Bar clinoforms	1.05	--	--	7.18	16.80	Fig. S3(M-N)
OM-Bar 22	Lower	Truncated	Bar clinoforms	0.60	--	--	3.70	8.66	Fig. S3(E)

OM-Bar 79	Lower	Truncated	Bar clinoforms	1.95	--	--	7.12	16.66	Fig. S3(O)
OM-Bar 39	Lower	Truncated	Bar clinoforms	0.97	--	--	9.19	21.50	Fig. S3(F)
OM-Bar 64	Upper	Truncated	Bar clinoforms	1.57	--	--	--	--	Fig. S3(J)
OM-Bar 65	Upper	Truncated	Bar clinoforms	0.79	--	--	--	--	Fig. S3(J)
OM-Bar 67	Upper	Truncated	Bar clinoforms	0.94	--	--	--	--	Fig. S3(L)
OM-Bar 68	Upper	Truncated	Bar clinoforms	1.41	--	--	--	--	Fig. S3(L)
OM-Bar 69	Upper	Truncated	Bar clinoforms	1.10	--	--	--	--	Fig. S3(L)
OM-Bar 70	Upper	Truncated	Bar clinoforms	2.04	--	--	--	--	Fig. S3(L)
OM-Bar 71	Upper	Truncated	Bar clinoforms	2.51	--	--	--	--	Fig. S3(L)
OM-Bar 72	Upper	Truncated	Bar clinoforms	1.10	--	--	--	--	Fig. S3(L)
OM-Bar 73	Upper	Truncated	Bar clinoforms	0.82	--	--	--	--	Fig. S3(L)
OM-Bar 01	Lower	Truncated	Bar clinoforms	1.20	--	--	--	--	Fig. S3(A)

OM-Bar 02	Lower	Truncated	Bar clinoforms	0.40	--	--	--	--	Fig. S3(B)
OM-Bar 03	Lower	Truncated	Bar clinoforms	0.20	--	--	--	--	Fig. S3(B)
OM-Bar 04	Lower	Truncated	Bar clinoforms	0.65	--	--	--	--	Fig. S3(B)
OM-Bar 05	Lower	Truncated	Bar clinoforms	0.40	--	--	--	--	Fig. S3(B)
OM-Bar 06	Lower	Truncated	Bar clinoforms	1.00	--	--	--	--	Fig. S3(B)
OM-Bar 07	Lower	Truncated	Bar clinoforms	0.60	--	--	--	--	Fig. S3(B)
OM-Bar 08	Lower	Truncated	Bar clinoforms	1.70	--	--	--	--	Fig. S3(B)
OM-Bar 09	Lower	Truncated	Bar clinoforms	0.25	--	--	--	--	Fig. S3(B)
OM-Bar 10	Lower	Truncated	Bar clinoforms	1.65	--	--	--	--	Fig. S3(B)
OM-Bar 11	Lower	Truncated	Bar clinoforms	0.20	--	--	--	--	Fig. S3(B)
OM-Bar 12	Lower	Truncated	Bar clinoforms	0.72	--	--	--	--	Fig. S3(C)
OM-Bar 13	Lower	Truncated	Bar clinoforms	0.48	--	--	--	--	Fig. S3(C)

OM-Bar 14	Lower	Truncated	Bar clinoforms	0.48	--	--	--	--	Fig. S3(C)
OM-Bar 15	Lower	Truncated	Bar clinoforms	0.32	--	--	--	--	Fig. S3(C)
OM-Bar 18	Lower	Truncated	Bar clinoforms	0.58	--	--	--	--	Fig. S3(D)
OM-Bar 19	Lower	Truncated	Bar clinoforms	0.60	--	--	--	--	Fig. S3(D)
OM-Bar 20	Lower	Truncated	Bar clinoforms	0.50	--	--	--	--	Fig. S3(E)
OM-Bar 21	Lower	Truncated	Bar clinoforms	0.35	--	--	--	--	Fig. S3(E)
OM-Bar 23	Lower	Truncated	Bar clinoforms	0.92	--	--	--	--	Fig. S3(F)
OM-Bar 24	Lower	Truncated	Bar clinoforms	0.33	--	--	--	--	Fig. S3(F)
OM-Bar 25	Lower	Truncated	Bar clinoforms	0.67	--	--	--	--	Fig. S3(F)
OM-Bar 26	Lower	Truncated	Bar clinoforms	0.50	--	--	--	--	Fig. S3(F)
OM-Bar 27	Lower	Truncated	Bar clinoforms	0.67	--	--	--	--	Fig. S3(F)
OM-Bar 28	Lower	Truncated	Bar clinoforms	0.33	--	--	--	--	Fig. S3(F)

OM-Bar 29	Lower	Truncated	Bar clinoforms	0.42	--	--	--	--	Fig. S3(F)
OM-Bar 30	Lower	Truncated	Bar clinoforms	0.30	--	--	--	--	Fig. S3(F)
OM-Bar 31	Lower	Truncated	Bar clinoforms	0.84	--	--	--	--	Fig. S3(F)
OM-Bar 32	Lower	Truncated	Bar clinoforms	1.14	--	--	--	--	Fig. S3(F)
OM-Bar 33	Lower	Truncated	Bar clinoforms	0.67	--	--	--	--	Fig. S3(F)
OM-Bar 34	Lower	Truncated	Bar clinoforms	0.47	--	--	--	--	Fig. S3(F)
OM-Bar 35	Lower	Truncated	Bar clinoforms	0.84	--	--	--	--	Fig. S3(F)
OM-Bar 36	Lower	Truncated	Bar clinoforms	0.67	--	--	--	--	Fig. S3(F)
OM-Bar 37	Lower	Truncated	Bar clinoforms	0.50	--	--	--	--	Fig. S3(F)
OM-Bar 38	Lower	Truncated	Bar clinoforms	0.92	--	--	--	--	Fig. S3(F)
OM-Bar 40	Lower	Truncated	Bar clinoforms	0.50	--	--	--	--	Fig. S3(F)
OM-Bar 41	Lower	Truncated	Bar clinoforms	0.58	--	--	--	--	Fig. S3(F)

OM-Bar 42	Lower	Truncated	Bar clinoforms	0.64	--	--	--	--	Fig. S3(F)
OM-Bar 43	Lower	Truncated	Bar clinoforms	0.24	--	--	--	--	Fig. S3(F)
OM-Bar 44	Lower	Truncated	Bar clinoforms	0.16	--	--	--	--	Fig. S3(F)
OM-Bar 45	Lower	Truncated	Bar clinoforms	0.24	--	--	--	--	Fig. S3(F)
OM-Bar 46	Lower	Truncated	Bar clinoforms	0.24	--	--	--	--	Fig. S3(F)
OM-Bar 47	Lower	Truncated	Bar clinoforms	0.48	--	--	--	--	Fig. S3(F)
OM-Bar 48	Lower	Truncated	Bar clinoforms	0.24	--	--	--	--	Fig. S3(F)
OM-Bar 50	Lower	Truncated	Bar clinoforms	0.47	--	--	--	--	Fig. S3(G)
OM-Bar 51	Lower	Truncated	Bar clinoforms	0.47	--	--	--	--	Fig. S3(G)
OM-Bar 52	Lower	Truncated	Bar clinoforms	0.50	--	--	--	--	Fig. S3(G)
OM-Bar 53	Lower	Truncated	Bar clinoforms	0.33	--	--	--	--	Fig. S3(G)
OM-Bar 54	Lower	Truncated	Bar clinoforms	0.38	--	--	--	--	Fig. S3(G)

OM-Bar 55	Lower	Truncated	Bar clinoforms	0.58	--	--	--	--	Fig. S3(G)
OM-Bar 56	Lower	Truncated	Bar clinoforms	0.63	--	--	--	--	Fig. S3(G)
OM-Bar 57	Lower	Truncated	Bar clinoforms	0.97	--	--	--	--	Fig. S3(G)
OM-Bar 58	Lower	Truncated	Bar clinoforms	1.26	--	--	--	--	Fig. S3(H)
OM-Bar 59	Lower	Truncated	Bar clinoforms	0.72	--	--	--	--	Fig. S3(I)
OM-Bar 60	Lower	Truncated	Bar clinoforms	0.18	--	--	--	--	Fig. S3(I)
OM-Bar 61	Lower	Truncated	Bar clinoforms	0.81	--	--	--	--	Fig. S3(I)
OM-Bar 62	Lower	Truncated	Bar clinoforms	0.94	--	--	--	--	Fig. S3(I)
OM-Bar 63	Lower	Truncated	Bar clinoforms	0.54	--	--	--	--	Fig. S3(I)
OM-Bar 75	Lower	Truncated	Bar clinoforms	0.65	--	--	--	--	Fig. S3(O)
OM-Bar 76	Lower	Truncated	Bar clinoforms	0.75	--	--	--	--	Fig. S3(O)
OM-Bar 77	Lower	Truncated	Bar clinoforms	0.75	--	--	--	--	Fig. S3(O)

OM-Bar 78	Lower	Truncated	Bar clinoforms	0.95	--	--	--	--	Fig. S3(O)
OM-Bar 80	Lower	Truncated	Bar clinoforms	0.61	--	--	--	--	Fig. S3(P)
OM-Bar 81	Lower	Truncated	Bar clinoforms	0.50	--	--	--	--	Fig. S3(P)
OM-Bar 82	Lower	Truncated	Bar clinoforms	0.50	--	--	--	--	Fig. S3(P)
OM-Bar 83	Lower	Truncated	Bar clinoforms	0.85	--	--	--	--	Fig. S3(P)
OM-Bar 84	Lower	Truncated	Bar clinoforms	1.10	--	--	--	--	Fig. S3(P)
OM-Bar 85	Lower	Truncated	Bar clinoforms	0.80	--	--	--	--	Fig. S3(P)
OM-Bar 86	Lower	Truncated	Bar clinoforms	0.40	--	--	--	--	Fig. S3(P)
OM-Bar 87	Lower	Truncated	Bar clinoforms	1.45	--	--	--	--	Fig. S3(P)
OM-Bar 88	Lower	Truncated	Bar clinoforms	0.65	--	--	--	--	Fig. S3(P)
OM-Bar 89	Lower	Truncated	Bar clinoforms	0.50	--	--	--	--	Fig. S3(P)
OM-Bar 90	Lower	Truncated	Bar clinoforms	0.40	--	--	--	--	Fig. S3(P)

OM-Bar 91	Lower	Truncated	Bar clinoforms	0.50	--	--	--	--	Fig. S3(P)
OM-Bar 92	Lower	Truncated	Bar clinoforms	0.30	--	--	--	--	Fig. S3(P)
OM-Bar 93	Lower	Truncated	Bar clinoforms	0.60	--	--	--	--	Fig. S3(P)
OM-Bar 94	Lower	Truncated	Bar clinoforms	0.60	--	--	--	--	Fig. S3(P)
OM-Bar 95	Lower	Truncated	Bar clinoforms	0.31	--	--	--	--	Fig. S3(P)
OM-Bar 96	Lower	Truncated	Bar clinoforms	0.30	--	--	--	--	Fig. S3(P)
OM-Bar 97	Lower	Truncated	Bar clinoforms	0.60	--	--	--	--	Fig. S3(P)
OM-Bar 98	Lower	Truncated	Bar clinoforms	0.60	--	--	--	--	Fig. S3(P)
OM-Bar 99	Lower	Truncated	Bar clinoforms	0.23	--	--	--	--	Fig. S3(Q)
OM-Bar 100	Lower	Truncated	Bar clinoforms	0.38	--	--	--	--	Fig. S3(Q)
OM-Bar 101	Lower	Truncated	Bar clinoforms	0.75	--	--	--	--	Fig. S3(Q)
OM-Bar 102	Lower	Truncated	Bar clinoforms	0.72	--	--	--	--	Fig. S3(Q)

OM-Bar 103	Lower	Truncated	Bar clinoforms	0.35	--	--	--	--	Fig. S3(Q)
OM-Bar 105	Lower	Truncated	Bar clinoforms	0.48	--	--	--	--	Fig. S3(R)
OM-Bar 106	Lower	Truncated	Bar clinoforms	1.05	--	--	--	--	Fig. S3(R)
OM-Bar 107	Lower	Truncated	Bar clinoforms	0.30	--	--	--	--	Fig. S3(R)
OM-Bar 108	Lower	Truncated	Bar clinoforms	0.30	--	--	--	--	Fig. S3(R)
OM-Bar 109	Lower	Truncated	Bar clinoforms	0.48	--	--	--	--	Fig. S3(R)

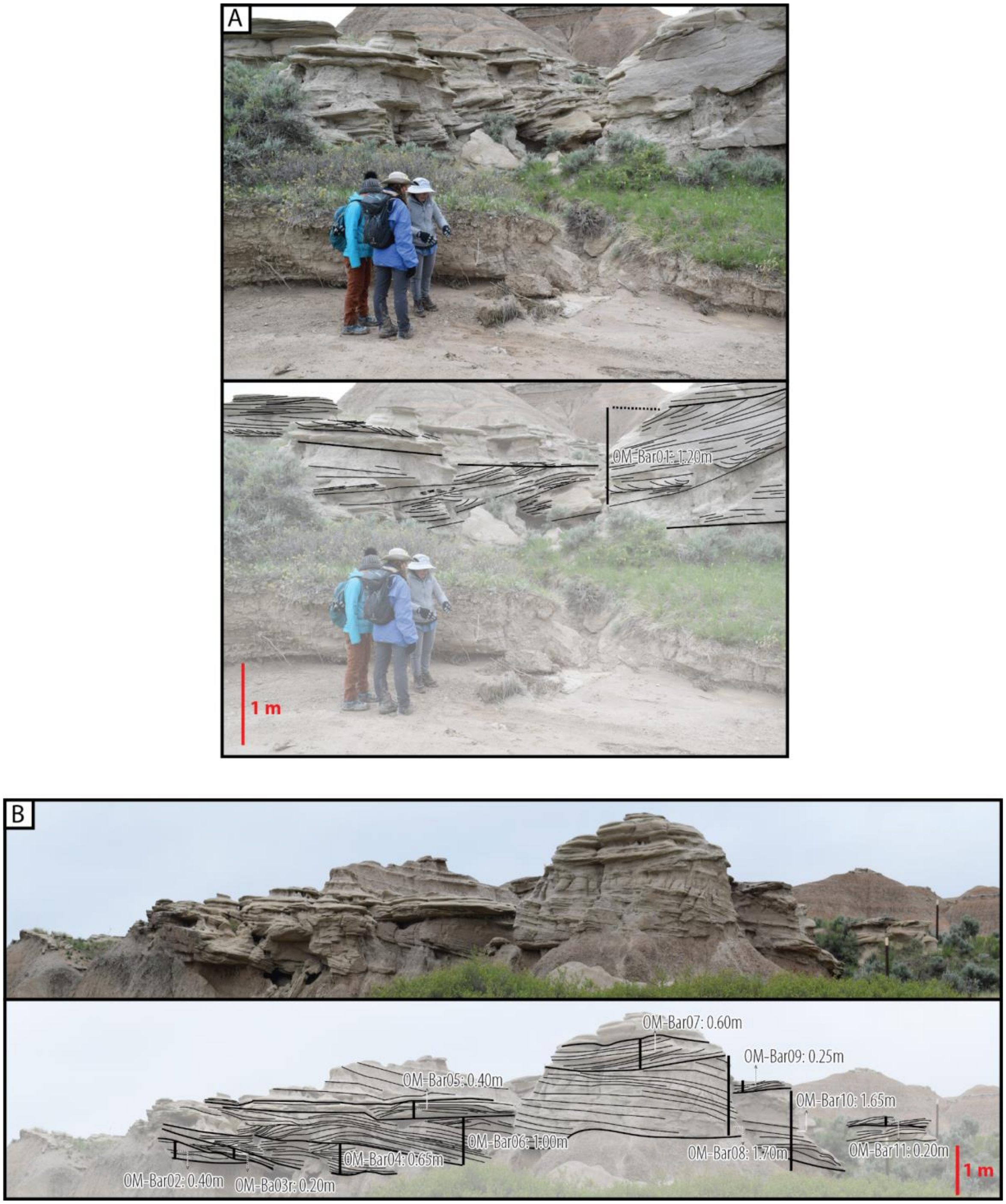

FIG. S3.— (A)-(B) Bar height and bar width results of Orella Member (OM).

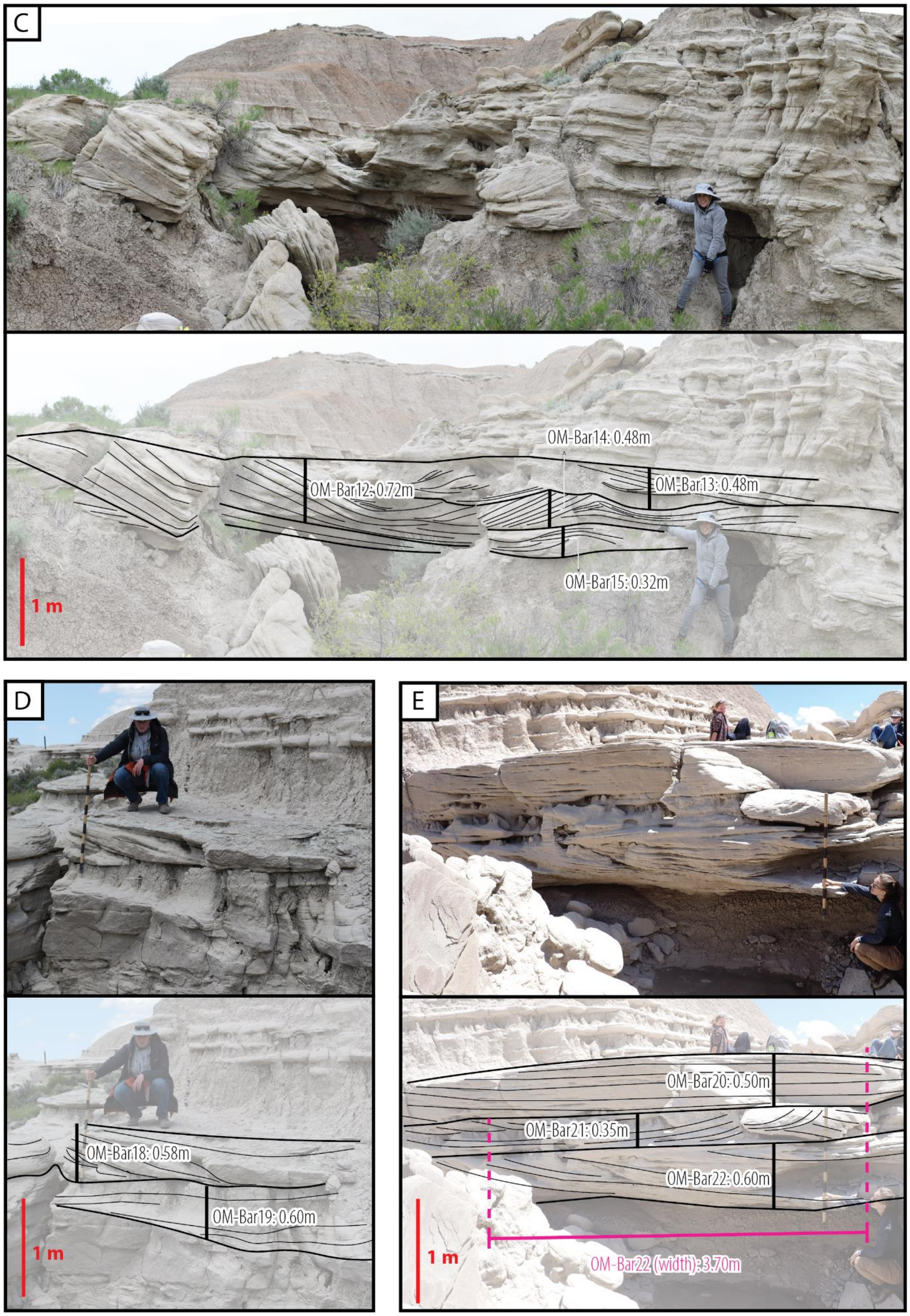

FIG. S-3. (cont.)— (C)-(E) Bar height and bar width results of Orella Member (OM).

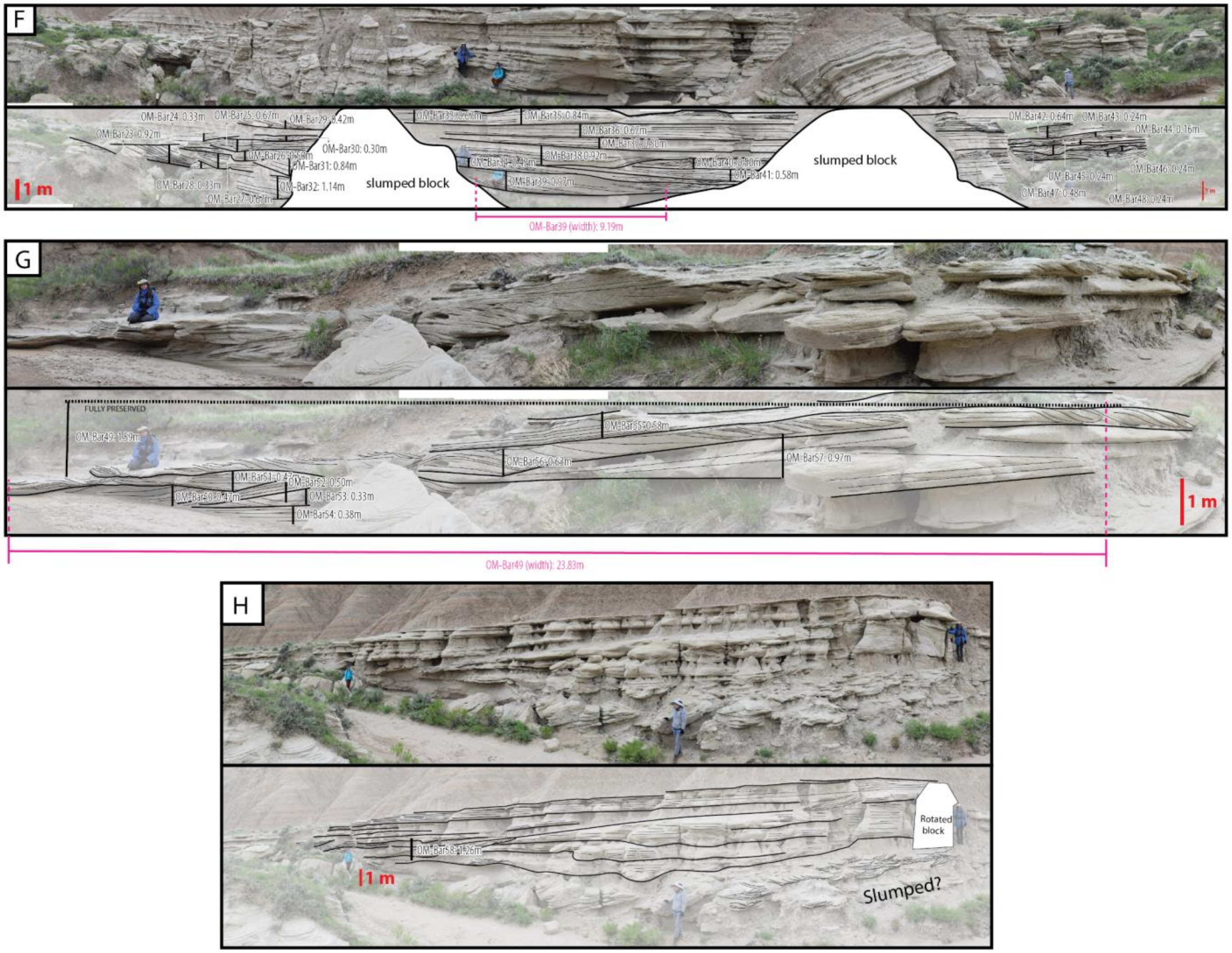

FIG. S-3. (cont.)— (F)-(H) Bar height and bar width results of Orella Member (OM).

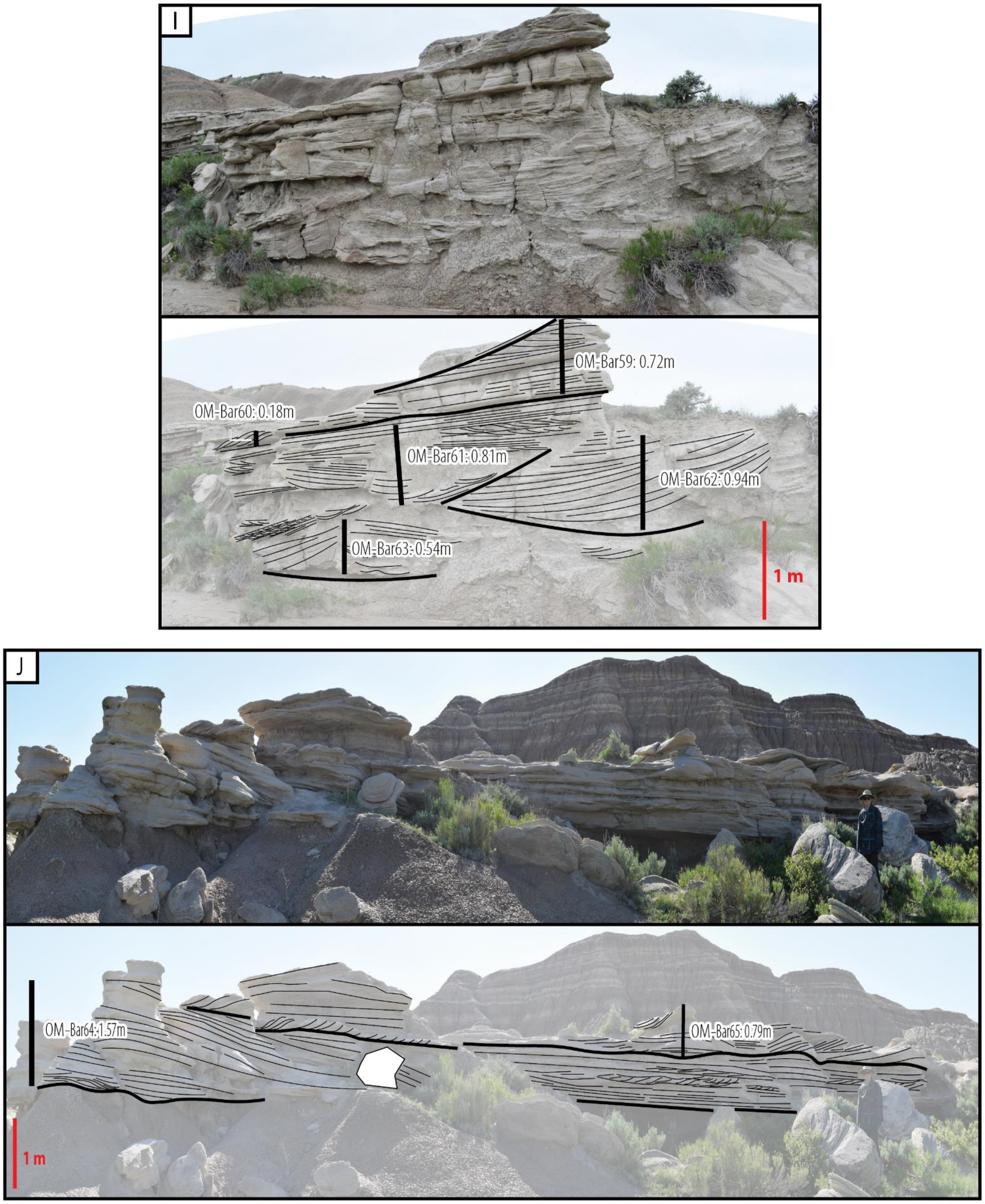

FIG. S-3. (cont.)— (I)-(J) Bar height and bar width results of Orella Member (OM).

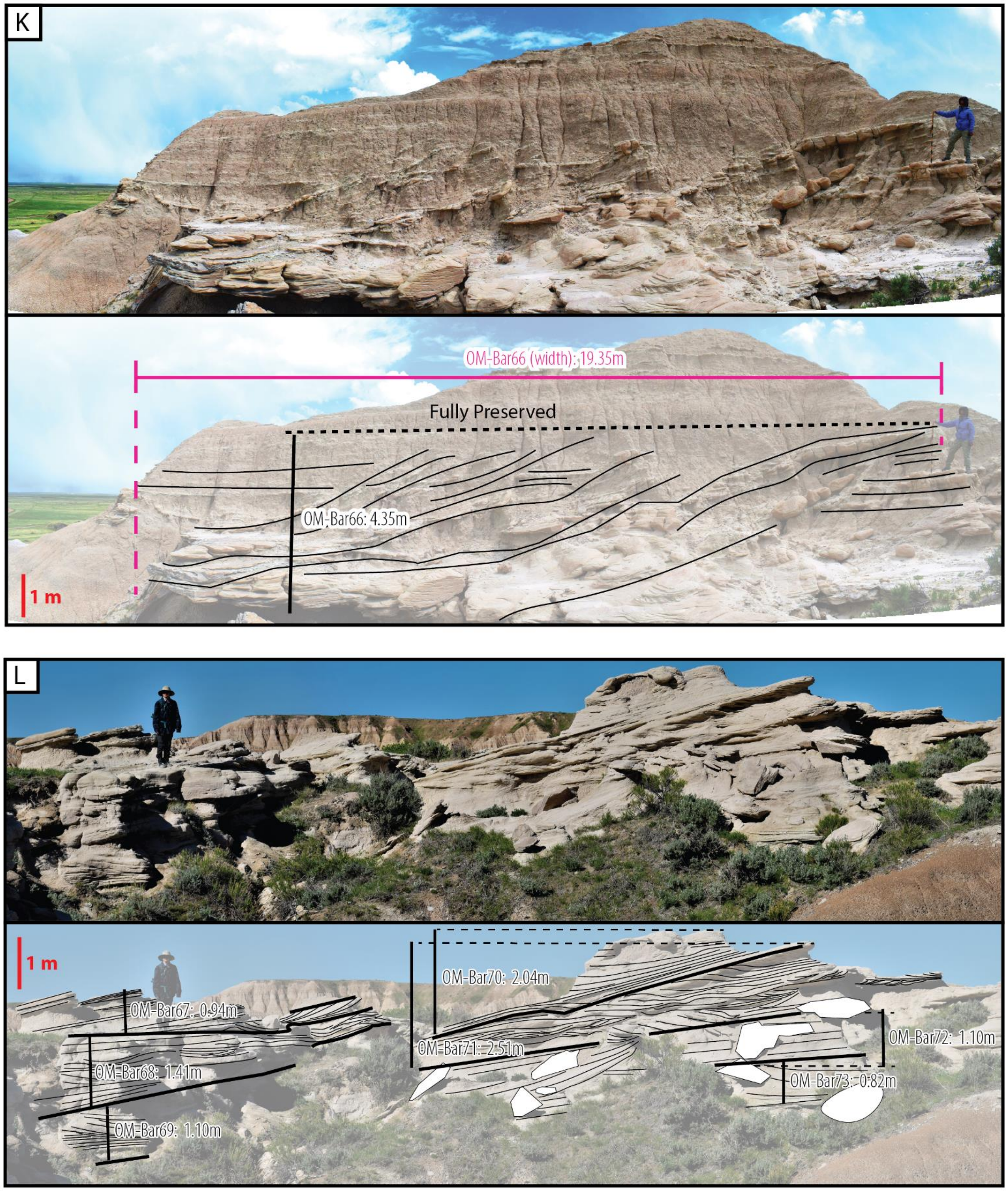

FIG. S-3. (cont.)— (K)-(L) Bar height and bar width results of Orella Member (OM).

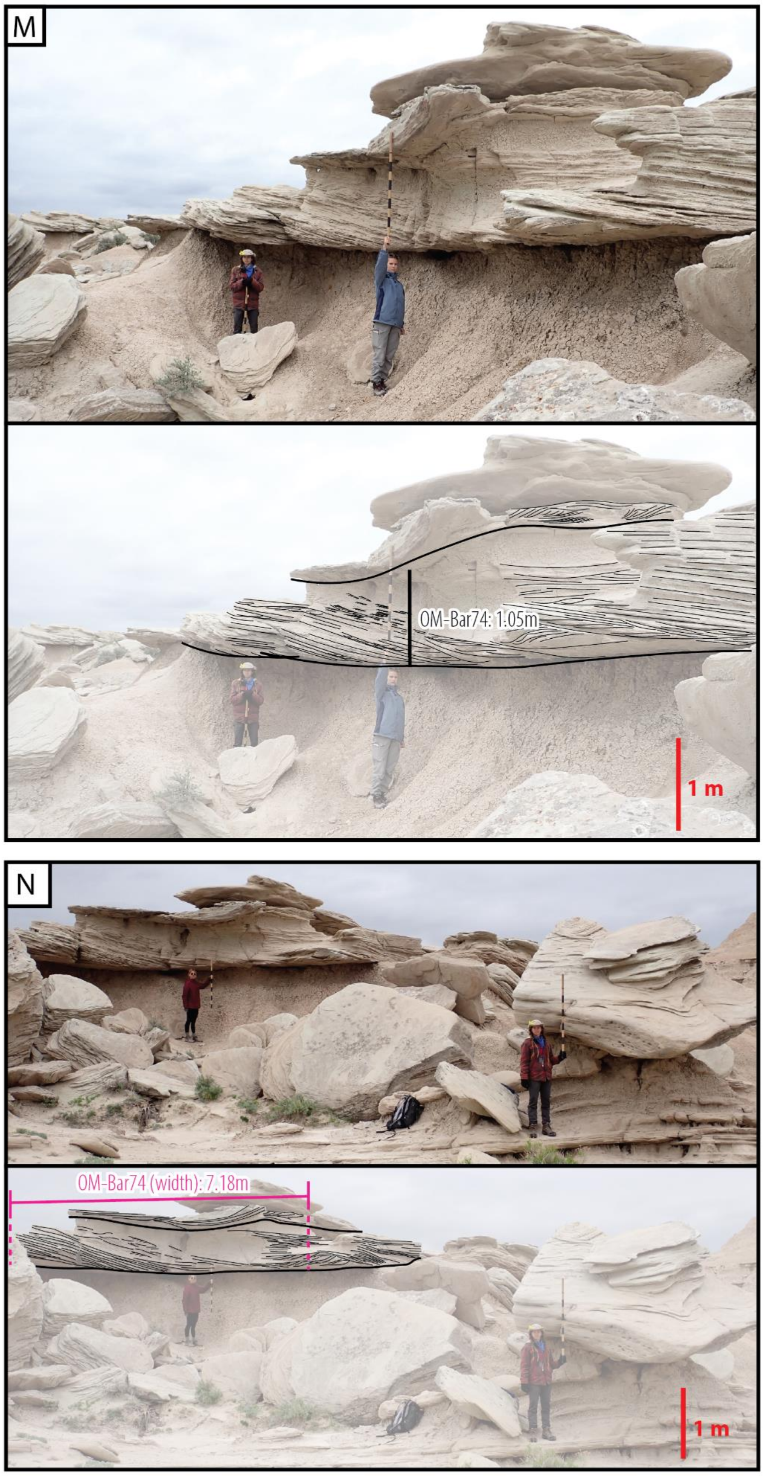

FIG. S-3. (cont.)— (M)-(N) Bar height and bar width results of Orella Member (OM).

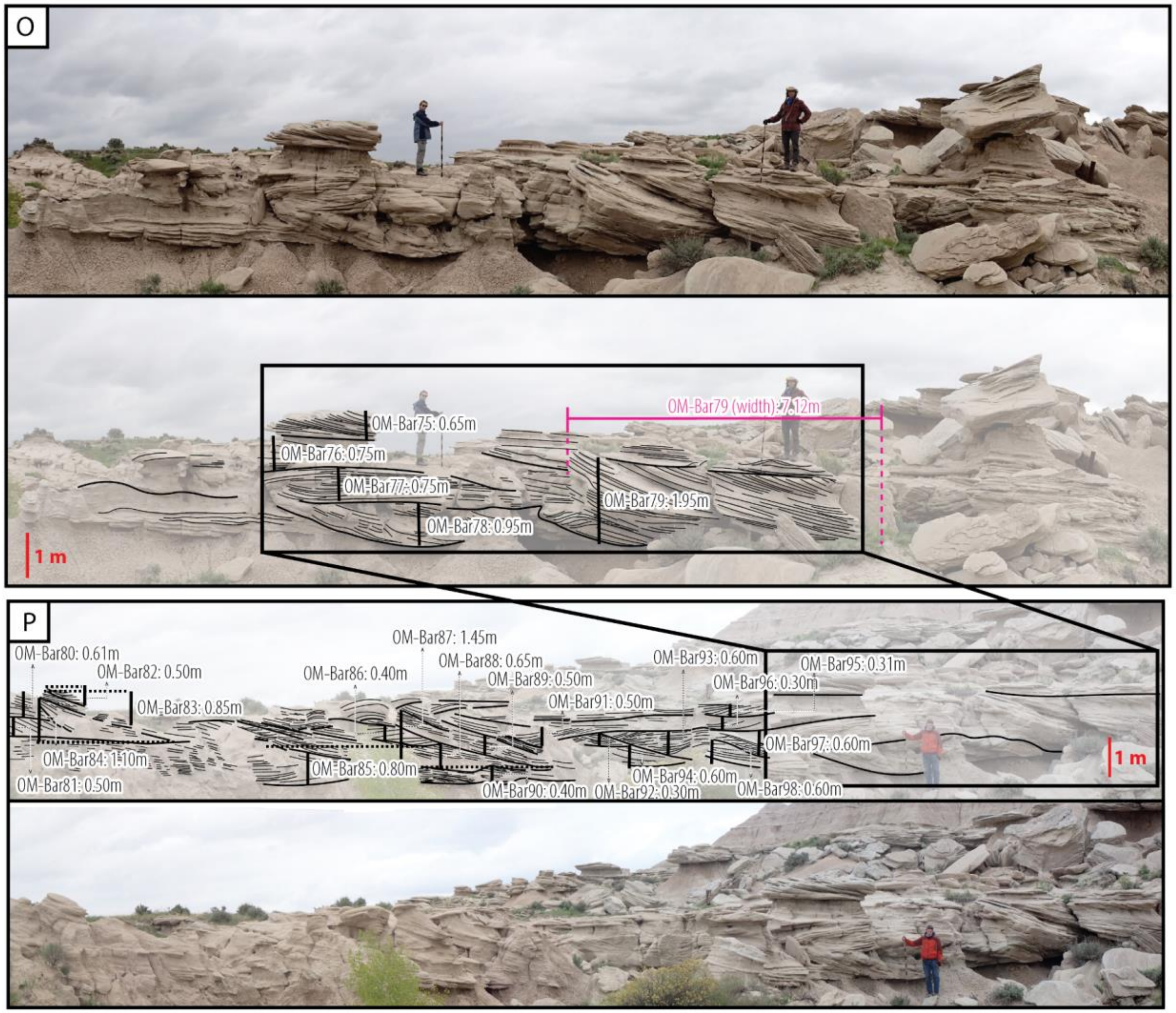

FIG. S-3. (cont.)— (O)-(P) Bar height and bar width results of Orella Member (OM).

FIG. S-3. (cont.)— (Q)-(R) Bar height and bar width results of Orella Member (OM).

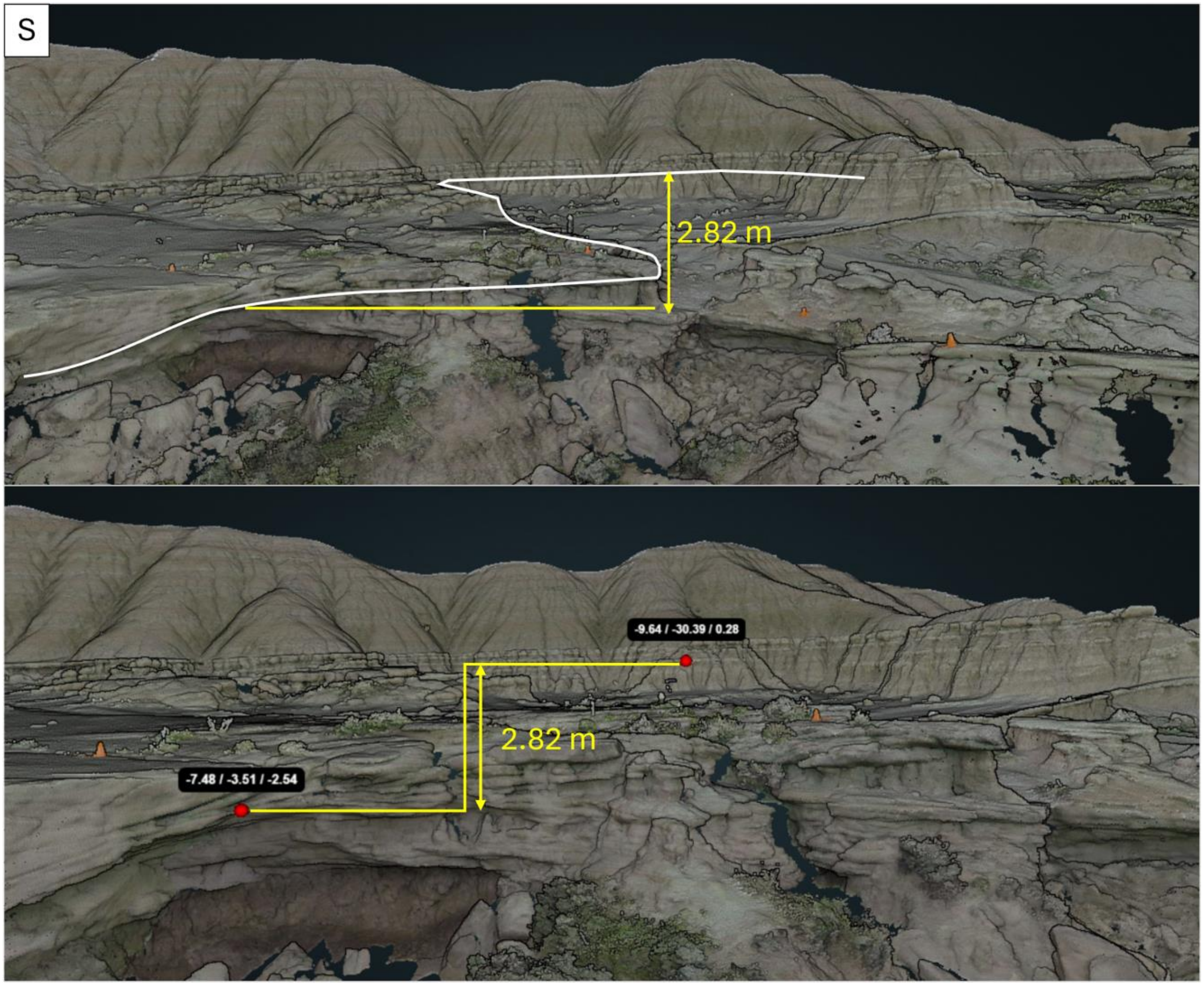

FIG. S-3. (cont.)— (S) Bar height and bar width results of Orella Member (OM).

Table S-3 - Cross-set Thicknesses

	Cross- set Thickness	Cross- set Thickness	Minimum bedform height (m)	Maximum bedform height (m)
	T_xbeds	T_xbeds	H_bed	H_bed
units	(cm)	(m)	(m)	(m)
formula used	-	-	H_bed = Txbeds(2.9 - 0.7)	H_bed = Txbeds(2.9 + 0.7)
method	measured in the field or from photographs	calculated	calculated	calculated
1	70	0.7	1.54	2.52
2	10	0.1	0.22	0.36
3	30	0.3	0.66	1.08
4	5	0.05	0.11	0.18
5	5	0.05	0.11	0.18
6	10	0.1	0.22	0.36
7	5	0.05	0.11	0.18
8	4.5	0.045	0.099	0.162
9	7	0.07	0.154	0.252
10	4.5	0.045	0.099	0.162
11	7	0.07	0.154	0.252
12	5	0.05	0.11	0.18
13	3	0.03	0.066	0.108
14	4	0.04	0.088	0.144
15	15	0.15	0.33	0.54
16	20	0.2	0.44	0.72
17	25	0.25	0.55	0.9
18	15	0.15	0.33	0.54

19	30	0.3	0.66	1.08
20	30	0.3	0.66	1.08
21	20	0.2	0.44	0.72
22	20	0.2	0.44	0.72
23	13	0.13	0.286	0.468
24	12	0.12	0.264	0.432
25	4	0.04	0.088	0.144
26	3	0.03	0.066	0.108
27	31	0.31	0.682	1.116
28	8	0.08	0.176	0.288
29	4	0.04	0.088	0.144
30	7	0.07	0.154	0.252
31	6	0.06	0.132	0.216
32	2	0.02	0.044	0.072
33	2	0.02	0.044	0.072
34	1	0.01	0.022	0.036
35	6	0.06	0.132	0.216
36	3	0.03	0.066	0.108
37	4	0.04	0.088	0.144
38	8	0.08	0.176	0.288
39	6	0.06	0.132	0.216
40	11	0.11	0.242	0.396
41	4	0.04	0.088	0.144
42	3	0.03	0.066	0.108
43	2	0.02	0.044	0.072
44	8	0.08	0.176	0.288
45	3	0.03	0.066	0.108
46	12	0.12	0.264	0.432
47	13	0.13	0.286	0.468
48	9	0.09	0.198	0.324

49	8	0.08	0.176	0.288
50	13	0.13	0.286	0.468
51	6	0.06	0.132	0.216
52	42	0.42	0.924	1.512
53	4	0.04	0.088	0.144
54	20	0.2	0.44	0.72
55	31	0.31	0.682	1.116
56	30	0.3	0.66	1.08
57	4	0.04	0.088	0.144
58	6	0.06	0.132	0.216
59	10	0.1	0.22	0.36
60	11	0.11	0.242	0.396
61	2	0.02	0.044	0.072
62	16	0.16	0.352	0.576
63	6	0.06	0.132	0.216
64	10	0.1	0.22	0.36
65	5	0.05	0.11	0.18
66	35	0.35	0.77	1.26
67	21	0.21	0.462	0.756
68	15	0.15	0.33	0.54
69	25	0.25	0.55	0.9
70	11	0.11	0.242	0.396
71	23	0.23	0.506	0.828
72	23	0.23	0.506	0.828
73	11	0.11	0.242	0.396
74	6	0.06	0.132	0.216
75	6	0.06	0.132	0.216
76	11	0.11	0.242	0.396
77	42	0.42	0.924	1.512
78	40	0.4	0.88	1.44

79	38	0.38	0.836	1.368
80	30	0.3	0.66	1.08
81	30	0.3	0.66	1.08
82	30	0.3	0.66	1.08
83	10	0.1	0.22	0.36
84	22	0.22	0.484	0.792
85	15	0.15	0.33	0.54
86	4	0.04	0.088	0.144
87	26	0.26	0.572	0.936
88	15	0.15	0.33	0.54
89	4	0.04	0.088	0.144
90	4	0.04	0.088	0.144
91	25	0.25	0.55	0.9
92	7	0.07	0.154	0.252
93	8	0.08	0.176	0.288
94	23	0.23	0.506	0.828
95	10	0.1	0.22	0.36
96	13	0.13	0.286	0.468
97	10	0.1	0.22	0.36
98	38	0.38	0.836	1.368
99	9	0.09	0.198	0.324
100	5	0.05	0.11	0.18
101	5	0.05	0.11	0.18
102	4	0.04	0.088	0.144
103	25	0.25	0.55	0.9
104	8	0.08	0.176	0.288
105	95	0.95	2.09	3.42
106	35	0.35	0.77	1.26
107	12	0.12	0.264	0.432
108	12	0.12	0.264	0.432

109	7	0.07	0.154	0.252
110	4	0.04	0.088	0.144
111	4	0.04	0.088	0.144
112	1	0.01	0.022	0.036
113	15	0.15	0.33	0.54
114	4	0.04	0.088	0.144
115	21	0.21	0.462	0.756
116	10	0.1	0.22	0.36
117	10	0.1	0.22	0.36
118	8	0.08	0.176	0.288
119	5	0.05	0.11	0.18
120	15	0.15	0.33	0.54
121	60	0.6	1.32	2.16
122	25	0.25	0.55	0.9
123	25	0.25	0.55	0.9
124	20	0.2	0.44	0.72
125	70	0.7	1.54	2.52

Table S-4 -Measurements and estimates associated with climbing bedforms

	Climb Angles (degrees) A	climb angle (radians) A	Bed thickness (cm) from field measurements or photographs H_layer	Vertical Translation rate of dunes (m/s) Vz	Deposition Rate from suspension Rd (m/s)	Deposition Rate from suspension R_d (cm/h)	Duration (hours) T_dep
method generated	field measurements or photographs	calculated	field measurements or photographs	calculated	calculated	calculated	calculated
formula				Vz = 2 (tan A)*Vx Vx = 0.0001	Rd = Vz * E_bed E_bed = 0.65		T_dep = H_layer/R_d
1	7	0.122111	28	0.00002637350	0.00000923073	3.32	8.43
2	9	0.157000	18	0.00003402006	0.00001190702	4.29	4.20
3	9	0.157000	18	0.00003402006	0.00001190702	4.29	4.20
4	9	0.157000	18	0.00003402006	0.00001190702	4.29	4.20
5	9	0.157000	29	0.00003402006	0.00001190702	4.29	6.77
6	15	0.261667	26	0.00005755304	0.00002014356	7.25	1.52
7	15	0.261667	55	0.00005755304	0.00002014356	7.25	5.10
8	16	0.279111	80	0.00006159008	0.00002155653	7.76	8.38
9	16	0.279111	26	0.00006159008	0.00002155653	7.76	3.35
10	17	0.296556	80	0.00006566769	0.00002298369	8.27	3.75
11	19	0.331444	20	0.00007395730	0.00002588506	9.32	1.82
12	21	0.366333	80	0.00008244847	0.00002885697	10.39	1.16
13	23	0.401222	20	0.00009117013	0.00003190955	11.49	1.74
14	23	0.401222	20	0.00009117013	0.00003190955	11.49	1.74

15	24	0.418667	55	0.00009562718	0.00003346951	12.05	0.83
16	25	0.436111	75	0.00010015396	0.00003505389	12.62	2.22
17	26	0.453556	75	0.00010475496	0.00003666424	13.20	2.12
18	26	0.453556	75	0.00010475496	0.00003666424	13.20	2.12
19	28	0.488444	26	0.00011419871	0.00003996955	14.39	0.90
20	33	0.575667	55	0.00013947172	0.00004881510	17.57	2.22
21	33	0.575667	0	0.00013947172	0.00004881510	17.57	0.00
22	34	0.593111	20	0.00014486118	0.00005070141	18.25	0.66
23	34	0.593111	75	0.00014486118	0.00005070141	18.25	1.26
24	34	0.593111	75	0.00014486118	0.00005070141	18.25	1.26
25	34	0.593111	75	0.00014486118	0.00005070141	18.25	1.26
26	34	0.593111	75	0.00014486118	0.00005070141	18.25	1.26
27	34	0.593111	75	0.00014486118	0.00005070141	18.25	1.26
28	34	0.593111	75	0.00014486118	0.00005070141	18.25	1.26
29	34	0.593111	75	0.00014486118	0.00005070141	18.25	1.26
30	34	0.593111	75	0.00014486118	0.00005070141	18.25	1.26
31	34	0.593111	75	0.00014486118	0.00005070141	18.25	1.26
32	34	0.593111	75	0.00014486118	0.00005070141	18.25	1.26
33	34	0.593111	75	0.00014486118	0.00005070141	18.25	1.26
34	35	0.610556	23	0.00015037891	0.00005263262	18.95	0.32
35	38	0.662889	55	0.00016778582	0.00005872504	21.14	1.66
36	38	0.662889	55	0.00016778582	0.00005872504	21.14	1.66
37	38	0.662889	55	0.00016778582	0.00005872504	21.14	1.66
38	38	0.662889	55	0.00016778582	0.00005872504	21.14	1.66
39	38	0.662889	55	0.00016778582	0.00005872504	21.14	1.66
40	38	0.662889	55	0.00016778582	0.00005872504	21.14	1.66
41	39	0.680333	23	0.00017390385	0.00006086635	21.91	0.41
42	42	0.732667	14	0.00019335673	0.00006767486	24.36	0.57
43	42	0.732667	14	0.00019335673	0.00006767486	24.36	0.57
44	42	0.732667	14	0.00019335673	0.00006767486	24.36	0.57

45	42	0.732667	50	0.00019335673	0.00006767486	24.36	0.53
46	42	0.732667	50	0.00019335673	0.00006767486	24.36	0.53
47	42	0.732667	50	0.00019335673	0.00006767486	24.36	0.53
48	42	0.732667	50	0.00019335673	0.00006767486	24.36	0.53

S-1. Laboratory-based Sedimentological Analysis

Samples (n=101) collected in the field were gently crushed using a mortar and pestle. The crushed sample was then disaggregated using a Q-sonica ultrasonic pulse generator which separated grains along partially cemented grain-grain boundaries. We assessed the effectiveness of sample disaggregation using a hand-lens, and repeated the process of sonication until the sample was fully disaggregated. The resulting disaggregated sediments were then separated into mud (< 62 µm), sand (62 µm- 2 mm) and gravel (> 2 mm), dried and weighed. The size-distributions of the different components were measured using a Horiba LA-960 Laser Particle Size Analyzer (LPSA). The distributions of the different components were then recombined using the weight fractions of mud, sand and gravel (Fig. 3D).

S-2. Laboratory-based Geochemical Analyses Methods

Geochemical analyses of 9 channel deposit samples and 23 floodplain samples were used for geochemical analyses. Samples were crushed with a mortar & pestle and/or a shatterbox until the mean particle size was 63 - 250 µm; this size range produces a high surface area and enough permeability for solvent to flow through the sample during extraction. Crushed samples were freeze dried overnight to remove excess moisture, minimize extraction time and reduce the risk of contamination. *n*-alkane extraction involved adding 200g of each sample soxhlet extractors and then flushing each sample with 300 mL 2:1 dichloromethane (DCM):methanol (MeOH) at 35 - 40°C for 24 - 48 hours.

The extracted samples were then processed through silica gel chromatographic columns to separate them into three 2 mL splits, first with hexane, then DCM, and then MeOH. Columns were prepared by adding 2 mL activated silica gel to 2 mL glass pipettes plugged with glass wool and vibrating the column until the silica gel settled as densely as possible. Straight-chained alkanes were isolated with urea adduction on the nonpolar fraction of biomarkers in hexane. The urea adduction involved evaporation of the solvent from each sample and adding 200 µL each of pentane, acetone, and a supersaturated urea:MeOH solution. This approach causes urea crystals to precipitate in the solution, trapping straight chained alkanes within them. Samples were frozen for a minimum of 30 minutes to stabilize the crystals, and then dried to remove any residual solution. The urea crystals were then rinsed with hexane and drained three times to remove any undesired organic compounds. Next, the crystals were dissolved in 1 mL of 1:1 MeOH:H_2O, added to 1 mL hexane and mixed for 60 seconds. The hexane layer was then extracted into an adduct vial. Urea adduction was applied a second time to the adducts of each sample, to further reduce the volume of any unwanted compounds. The n-alkane values for each sample were obtained by measuring the final adducts on a Thermo Scientific TRACE Gas Chromatograph Ultra and the ^{2}H and ^{13}C values were obtained by measuring the adducts on a GC-Mass spectrometer.

Table S-5 - Modern river δD from (Kendall and Coplen, 2001)

Degrees Latitude	Degrees Longitude	Drainage Area (sq. km)	Altitude km	Mean river δD (‰)
37.31	-95.11	12703.95	0.246888	-37
41.29	-96.28	17871	0.336804	-59
39.1	-96.6	10.36		-44
41.78	-100.53	2486.4	0.85344	-74
45.51	-100.82	13908.3	0.4965192	-91
45.26	-100.84	12639.2	0.5062728	-91
44.37	-102.57	18673.9	0.6620256	-109
44.01	-103.83	214.97	1.801368	-123
37.08	-105.76	19943	2.2640544	-100
39.17	-106.39	62.16	2.996184	-129
41.02	-106.82	189.07	2.520696	-131

Table S-6: Modern River Hydrology

River Name	Gage Number	Latitude	Longitude	Elevation of Gage (m above sea level)	Mean Catchment Elevation (m above sea level)	Median gage discharge (cms)	Stream Length (km)	Longitudinal slope (m/m)	Catchment Averaged Mean Annual Precipitation (cm)	Catchment Relief (m)	Drainage area (sq. Km)	comments
NorthLoup	6785500	41.941667	-99.860278	753.54	939.95	13.99	133.06	0.00	NA	267	4738	no precipitation gages in catchment
NorthLoup	6786000	41.776944	-99.379167	687.16	904.95	16.59	179.80	0.00	54.08	308	5956	
NorthLoup	6788500	41.606361	-98.919694	615.03	847.03	25.40	229.67	0.00	55.78	403	9594	
NorthLoup	6788988	41.502222	-98.796389	606.55	648.29	0.06	17.36	0.00	NA	40	158	no precipitation gages in catchment
NorthLoup	6790500	41.263333	-98.448889	538.58	819.57	28.60	288.94	0.00	55.94	458	10958	
Niobrara	6454100	42.423611	-103.792222	1344.47	1497.79	0.37	87.96	0.00	38.89	161	2383	continuous series unavailable, daily average discharges used
Niobrara	6461500	42.902078	-100.362528	699.96	1163.40	23.13	389.83	0.00	42.39	849	21505	
Niobrara	6463720	42.780556	-99.339722	548.59	1097.66	40.49	479.03	0.00	44.96	1032	25922	
Niobrara	6465500	42.739722	-98.222778	401.65	1160.88	55.22	575.67	0.00	48.68	1183	32978	

Calamus	6787500	41.810278	-99.183056	658.95	775.58	8.41	106.29	0.00	57.60	182	2581	Discharge File clipped to remove any influence of the Virginia Smith Dam. Series is from daily averages rather than continuous time series
Calamus	6787000	41.947	-99.386028	693.29	793.98	7.28	128.96	0.00	NA	221	1861	no precipitation gages in catchment
Platte	6679500	41.926944	-103.813611	1200.14	2023.93	14.89	587.13	0.00	54.41	1745	62271	continuous series unavailable, daily average discharges used
Platte	6687500	41.316667	-102.125833	1005.95	1902.79	36.81	744.69	0.00	53.92	1997	74257	continuous series unavailable, daily average discharges used
Platte	6691000	41.21	-101.117222	891.36	1864.61	4.54	832.50	0.00	52.97	2101	77538	continuous series unavailable, daily average discharges used
Platte	6768000	40.6825	-99.540556	702.54	1789.63	34.55	980.76	0.00	53.24	2316	148322	
Platte	6768025	40.678889	-99.489167	696.68	1788.57	4.87	985.06	0.00	53.24	2321	148471	

Platte	6768035	40.685556	-99.438889	690.60	1787.96	24.47	989.20	0.00	53.24	2326	148556	
Platte	6805500	41.014978	-96.1575	311.63	1429.59	207.85	1341.10	0.00	56.77	2672	219695	
Republica n	6837000	40.187778	-100.618611	754.39	1184.02	1.31	281.89	0.00	43.92	941	31856	
Republica n	6843500	40.284444	-100.143611	685.71	1136.37	3.57	322.75	0.00	46.20	1010	37420	
Ninnescah	7144910	37.637778	-98.720556	558.14	608.25	0.22	28.15	0.00	64.33	82	311	
Ninnescah	7145200	37.561667	-97.852778	415.71	533.15	3.77	117.05	0.00	66.70	226	1513	
Ninnescah	7145500	37.456964	-97.423556	374.59	511.19	5.52	164.35	0.00	68.08	267	5651	

Table S-7: Geochemical proxy data

Sample	Latitude	Longitude	Elevation (m)	Depositional environment	d2H	d13C	ACL	CPI
BM-TGPB1-001	42.85587	-103.58669	1170	channel	-165.74	-30.1	29.28	5.91
BM-TGPB1-002	42.85587	-103.58669	1170	channel	-157.42	-	29.23	5.64
BM-TGPB1-003	42.85587	-103.58669	1170	channel	-162.95	-27.7	29.25	5.99
BM-TGPB1-004	42.85587	-103.58669	1170	channel	-150.79	-28.1	-	-
BM-TGPB1-005	42.85587	-103.58669	1170	channel	-159.55	-27.7	29.22	5.6
BM-TGPB2-011	42.85577	-103.58648	1171	channel	-	-	29.2	5.53
BM-TGPB3-012	42.85581	-103.58639	1170	channel	-154.46	-27.5	29.56	6.26
BM-TGPB3-013	42.85581	-103.58639	1170	channel	-161.87	-26.6	29.04	5.05
BM-TGPB3-014	42.85581	-103.58639	1170	channel	-170.34	-29.4	29.45	5.6
BM-TGPB1-006	42.85587	-103.58669	1170	floodplain	-158.13	-28	29.55	5.76
BM-TGPB1-007	42.85587	-103.58669	1170	floodplain	-160.18	-27.7	28.73	4.53
BM-TGPB2-008	42.85577	-103.58646	1171	floodplain	-159.14	-27.8	29.25	5.57
BM-TGPB2-009	42.85577	-103.58648	1171	floodplain	-162.95	-28.9	28.63	4.88
BM-TGPB2-010	42.85577	-103.58648	1171	floodplain	-164.37	-28.8	29.41	6.33
BM-TGPB3-015	42.85581	-103.58639	1170	floodplain	-151.99	-29	29.27	5.85